Politecnico di Milano

SCUOLA DI INGEGNERIA INDUSTRIALE E DELL'INFORMAZIONE
Dipartimento di Scienze e Tecnologie Aerospaziali
Master of Science – Aeronautical Engineering, Aerodynamics

POLITECNICO
MILANO 1863

Validation and modification of the Valarezo-Chin method for the prediction of maximum lift

Advisor
Prof. Maurizio Boffadossi

Candidate
Demetrio Pibiri
ID 928637

Academic Year 2020/21

"Our greatest weakness lies in giving up.
The most certain way to succeed is always to try just one more time."
Thomas Edison

Acknowledgements

I deeply thank professor Boffadossi, a kind and gentle man, for the great help given.

Special thanks to my father and my mother for the support and the love given during all my university studies and difficulty periods. Thanks also to my sister, since she would be offended if I don't mention her.

Abstract

The research and the calculation of the **maximum lift coefficient** of the aircraft wings, are as complex, due to the complicated nonlinear behaviour of flow physics, as important, to avoid the dangerous phenomenon of **stall**, linked to it.

Predicting this parameter already in the pre-conceptual phase of aircraft design, is fundamental, in order to start the project with the choice of the most suitable two-dimensional airfoils. Despite this, there are only few not totally empirical methods for the prediction of maximum lift, which are able to combine simplicity, low computational cost and accuracy of results.

One of these is the **pressure difference rule**, theorised by engineers and AIAA members Valarezo and Chin, which pairs the recurrence of an empirical phenomenon, observed during airfoils stall in a wind tunnel, with a panel method, i.e. *low-fidelity* CFD.

In this thesis, the operation of this interesting method has been analysed and its effectiveness has been verified, on a small number of NACA airfoils, at fixed Reynolds and Mach numbers. The study was carried out using **XFOIL**, a program created by engineer Drela, for the calculation of two-dimensional and subsonic aerodynamic problems, based on the panel method.

Finally, given the low accuracy of the results, obtained from the analysis of the **Valarezo-Chin method**, a modification to this method is proposed, based on the dependence of aforementioned results on the shape of the airfoils: the data produced by this new method are better, but less reliable, since the small number of airfoils analysed.

Keywords: prediction, maximum lift coefficient, stall angle, stall, pressure difference rule, Valarezo-Chin method, NACA airfoils, XFOIL.

Abstract in lingua italiana

La ricerca e il calcolo del **coefficiente di massima portanza** dell'ala di un aeromobile sono tanto complessi, per il complicato comportamento non lineare della fisica del flusso, quanto importanti, per evitare il pericoloso fenomeno dello **stallo**, ad esso legato.

Prevedere tale parametro già nella fase preconcettuale di progettazione dell'aeromobile, è fondamentale al fine di avviare al meglio il progetto con la scelta dei profili alari bi-dimensionali più adatti. Nonostante ciò, sono pochi i metodi non totalmente empirici per la previsione della portanza massima, che associano semplicità, basso costo computazionale e precisione dei risultati.

Uno di questi è la **regola della differenza di pressione**, teorizzata dagli ingegneri e membri dell'AIAA Valarezo e Chin, la quale combina la ricorrenza di un fenomeno empirico osservato durante lo stallo dei profili alari in galleria del vento, con un metodo a pannelli, ovvero *low-fidelity* CFD.

Nella tesi è stato analizzato il funzionamento ed è stata verificata l'efficacia di questo interessante metodo su un piccolo numero di **profili NACA**, a numeri di Reynolds e Mach fissati. Lo studio è stato svolto grazie all'utilizzo di **XFOIL**, un programma, realizzato dell'ingegner Drela, per il calcolo di problemi aerodinamici bi-dimensionali e subsonici, basato su metodo a pannelli.

Infine, vista la bassa accuratezza dei risultati ottenuti dall'analisi del **metodo di Valarezo-Chin**, è stata proposta una modifica ad esso, basata sulla dipendenza dei suddetti risultati dalla forma dei profili: i dati prodotti da questo nuovo criterio risultano migliori, ma meno affidabili, dato lo scarso numero di profili analizzati.

Parole chiave: previsione, coefficiente di massima portanza, angolo di stallo, stallo, regola della differenza di pressione, metodo di Valarezo-Chin, profili NACA, XFOIL.

Contents

Acknowledgements **iii**

Abstract **iv**

Abstract in lingua italiana **v**

Contents **vi**

List of Figures **viii**

List of Tables **xi**

1 Introduction **1**
1.1 Thesis outline 2

2 Maximum lift coefficient and stall **3**
2.1 Maximum Lift Coefficient 3
2.2 Stall 4

3 NACA airfoils **8**
3.1 4-digit Series 8
3.2 5-digit Series 9
3.3 Laminar 6-digit Series 11

4 XFOIL **14**
4.1 Inviscid Formulation 14
4.2 Viscous Formulation 16
4.3 Inviscid-Viscous Coupling 17
4.4 Solution 18
4.5 Karman-Tsien Compressibility Correction 18

5 Valarezo-Chin Method **19**

6 Verification of the method **21**
6.1 Variability of XFOIL results 23
6.2 Comparison with experimental data 24
6.3 Validity check of the Valarezo-Chin method 25

6.4 Pressure difference rule application 27

7 Modification of the method **41**
7.1 Thin airfoils 41
7.2 Thick airfoils 44
7.3 Modified pressure difference rule application 46

Conclusions **50**

Bibliography **51**

Sitography **53**

Appendix **54**
.1 MATLAB script for the pressure difference rule implementation . . . 54

List of Figures

Figure 2.1 Lift coefficient vs angle of attack curve for a NACA 23012, obtained through XFOIL 3
Figure 2.2 Boundary layer speed profiles on the NACA 0012 airfoil, showing the adverse pressure gradient effect which causes the separation . 4
Figure 2.3 Typical evolution of the NACA0012 pressure distribution, respectively at $\alpha = 5°$, $\alpha = 10°$ and $\alpha = 15°$, computed by XFOIL . . 5
Figure 2.4 NACA0012 pressure distribution at the stall condition, i.e. $\alpha = 18.5° = \alpha_{stall}$, computed by XFOIL 6
Figure 2.5 Flow behaviour the different stall types [5] 7
Figure 2.6 Typical lift coefficient polars for the different stall types [6] . . 7

Figure 3.1 NACA 4-digits airfoils 12
Figure 3.2 NACA 5-digits airfoils 13
Figure 3.3 NACA 6-digits airfoils 13

Figure 4.1 Airfoil and wake paneling with vorticity and source distributions, with trailing edge details 15

Figure 5.1 Pressure difference rule for maximum lift [12] 19
Figure 5.2 Example of pressure difference rule usage on a 3D wing [12] . . 20

Figure 6.1 Collection of the maximum lift coefficients of all the airfoils included in Abbott and Von Doenhoff's report [2], in relation to their ideal lift coefficients, i.e. the C_L for which the airfoil is designed. . . . 22
Figure 6.2 n_{panel} parameterization on lift coefficient versus angle of attack plot 30
Figure 6.3 $\Delta\alpha$ parameterization on lift coefficient versus angle of attack plot 31
Figure 6.4 N_{crit} parameterization on lift coefficient versus angle of attack plot 32
Figure 6.5 NACA0006 C_L-α curve comparison between experimental and computational data 33
Figure 6.6 NACA0009 C_L-α curve comparison between experimental and computational data 33
Figure 6.7 NACA0012 C_L-α curve comparison between experimental and computational data 34

Figure 6.8 NACA1412 C_L-α curve comparison between experimental and computational data . . . 34
Figure 6.9 NACA2412 C_L-α curve comparison between experimental and computational data . . . 35
Figure 6.10 NACA2424 C_L-α curve comparison between experimental and computational data . . . 35
Figure 6.11 NACA4412 C_L-α curve comparison between experimental and computational data . . . 36
Figure 6.12 NACA4424 C_L-α curve comparison between experimental and computational data . . . 36
Figure 6.13 NACA23012 C_L-α curve comparison between experimental and computational data . . . 37
Figure 6.14 NACA23021 C_L-α curve comparison between experimental and computational data . . . 37
Figure 6.15 NACA23024 C_L-α curve comparison between experimental and computational data . . . 38
Figure 6.16 NACA64-208 C_L-α curve comparison between experimental and computational data . . . 38
Figure 6.17 NACA64_1-212 C_L-α curve comparison between experimental and computational . . . 39
Figure 6.18 NACA64_4-221 C_L-α curve comparison between experimental and computational . . . 39
Figure 6.19 Pressure difference rule digitized with *WebPlotDigitizer* . . . 40

Figure 7.1 $|\Delta C_p|$ data from the Table 6.2 . . . 42
Figure 7.2 $|\Delta C_p|$ data from the Table 6.3 . . . 42
Figure 7.3 $|\Delta C_p|$ data from the Table 6.2 . . . 42
Figure 7.4 $|\Delta C_p|$ data from the Table 6.3 . . . 42
Figure 7.5 Plot of $|\Delta C_p|_{\alpha}^{init}$ versus maximum camber: first step of the modified criterion to predict the α_{stall} . . . 43
Figure 7.6 Plot of $|\Delta C_p|_{C_L}^{init}$ versus maximum camber: first step of the modified criterion to predict the $C_{L\,max}$ . . . 43
Figure 7.7 Plot of amplification factor versus maximum thickness: second step of the modified criterion to predict the α_{stall} . . . 43
Figure 7.8 Plot of amplification factor versus maximum thickness: second step of the modified criterion to predict the $C_{L\,max}$ . . . 43
Figure 7.9 $|\Delta C_p|$ data from the Table 6.2 . . . 44
Figure 7.10 $|\Delta C_p|$ data from the Table 6.3 . . . 44
Figure 7.11 $|\Delta C_p|$ data from the Table 6.2 . . . 44
Figure 7.12 $|\Delta C_p|$ data from the Table 6.3 . . . 44
Figure 7.13 Plot of $|\Delta C_p|_{\alpha}^{init}$ versus maximum camber: first step of the modified criterion to predict the α_{stall} . . . 45

Figure 7.14 Plot of $|\Delta C_p|_{C_L}^{init}$ versus maximum camber: first step of the modified criterion to predict the $C_{L\,max}$ 45
Figure 7.15 Plot of amplification factor versus maximum thickness: second step of the modified criterion to predict the α_{stall} 45
Figure 7.16 Plot of amplification factor versus maximum thickness: second step of the modified criterion to predict the $C_{L\,max}$ 45
Figure 7.17 NACA1410 process diagram of the modified pressure difference rule 46
Figure 7.18 NACA1410 stall prediction with the modified method compared with the experimental data by Abbott and and Von Doenhoff 46
Figure 7.19 NACA2408 process diagram of the modified pressure difference rule 47
Figure 7.20 NACA2408 stall prediction with the modified method compared with the experimental data by Abbott and and Von Doenhoff 47
Figure 7.21 NACA2421 process diagram of the modified pressure difference rule 48
Figure 7.22 NACA2421 stall prediction with the modified method compared with the experimental data by Abbott and and Von Doenhoff 48
Figure 7.23 NACA4421 process diagram of the modified pressure difference rule 49
Figure 7.24 NACA4421 stall prediction with the modified method compared with the experimental data by Abbott and and Von Doenhoff 49

List of Tables

Table 3.1 Table of NACA 5-Digits values with simple camber line 10
Table 3.2 Table of NACA 5-Digits values with reflexed camber line 10

Table 6.1 Comparison between Abbott and Von Doenhoff's experimental data and XFOIL results for the stall 24
Table 6.2 C_p difference between suction peak and trailing edge for the Abbott and Von Doenhoff's stall angle, computed by XFOIL 25
Table 6.3 C_p difference between suction peak and trailing edge for the XFOIL stall conditions, computed by XFOIL 26
Table 6.4 C_p difference between suction peak and trailing edge corresponding to the Abbott and Von Doenhoff's maximum lift coefficient, computed by XFOIL 27
Table 6.5 Comparison between the experimental stall and the inviscid prevision of the stall, obtained with the *pressure difference rule* . . . 28
Table 6.6 Comparison between the experimental stall and the viscous prevision of the stall, obtained with the *pressure difference rule* . . . 28

Chapter 1

Introduction

One of the fundamental performance indicators of an aircraft flight phases is the maximum lift coefficient, significant particularly in take-off and landing phases. Knowing this parameter during the conceptual design has always been important, in order to choose the proper airfoil, according to the aircraft requirements and missions, and to avoid the stall condition associated with it.

In commercial transport sector, especially during the preliminary project of the aircraft, a reduction in overall cost, expressed both in time and resources, is often preferred, at expense of precision and reliability of results. Moreover, the study and the predictability of the maximum lift coefficient are very complex, due to intricate non-linear flow physics surrounding it. Indeed, the analytical estimation of this performance indicator seems to be challenging, even with the expensive high order computational fluid dynamics (CFD): the typical errors stand between 5% and 9%, if the correct turbulence models are applied [8, 9]. Therefore, since also wind tunnel tests are too expensive at a conceptual design stage, the common trend is to use empirical approaches and cheap design methods, even if they may not yield results reliable enough to predict the stall.

The declared aim of the Valarezo and Chin report is to develop a hybrid method that couples inexpensive-to-run CFD technology with a physical criterion, derived from observations made during wind-tunnel testing [12].

The research goal of the thesis is to verify the validity of the *pressure difference rule*, theorized by Valarezo and Chin; this analysis is carried out specifically for certain bi-dimensional airfoils at determined flow conditions. In order to fill the lacks and inaccuracies that the method presents, a modification to it is proposed.

1.1 Thesis outline

Firstly, in chapter 2, a general background of maximum lift and stall physical phenomena is given. In the third chapter (3), a description of the airfoils considered in the thesis, i.e. the NACA airfoils, is reported. Subsequently, the chapter 4 describes the operation of XFOIL, the medium-fidelity program used for the aerodynamic computations in the thesis. A brief overview of the Valarezo and Chin method is outlined in chapter 5. Then, the method is analyzed and verified in chapter 6 and the modification is presented in the following one (7). In the last chapter conclusions and final considerations are highlighted.

Chapter 2

Maximum lift coefficient and stall

Since this thesis is about the prediction of the maximum lift coefficient of two dimensional airfoils, it is considered important to give a primary definition of this performance indicator and the main physical phenomena behind it. To write this chapter, reference has been made to the master thesis of Balraj Singh [10], in addition to the book *"Introduction to Transonic Aerodynamics"* by Roelof Vos and Saeed Farokhi [14] and the report *"Examples of three representative types of airfoil-section stall at low speed"* by G. B. Mccullough and D. Gault [7].

2.1 Maximum Lift Coefficient

The lift coefficient (C_L) is a dimensionless coefficient which models all of the complex dependencies between the lifting capabilities of an aerodynamic body and its shape, its inclination and flow conditions around it.

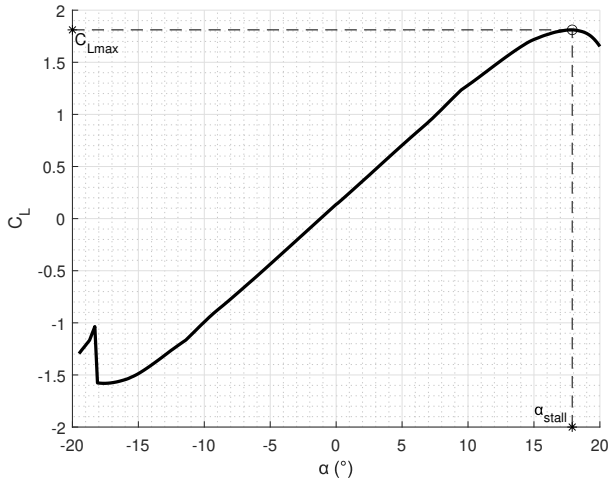

Figure 2.1. Lift coefficient vs angle of attack curve for a NACA 23012, obtained through XFOIL

The most important characteristic of this coefficient is its linear growing with increasing angle of attack α, as shown in Figure 2.1. However, at a certain point, the boundary layer, which until then has been attached to the aerodynamic shape of the airfoil, starts to separate from the upper surface of the wing; further increasing the incidence, this separation gets worse and this implies the loss of the linear behaviour and a resulting reduction of the growth rate.

The angle α_{stall}, in which this rate reduces to zero, sets out the **maximum lift coefficient** $C_{L\,max}$ and it corresponds to the so-called **stall**, i.e. the condition in which the aerodynamic body reaches its maximum lifting capability and after which it starts to lose lift. At this state, the flow on the upper side of the wing is completely separated and this leads to an increase in drag. Therefore, since it's due to the growing importance of the viscous effects, the maximum lift coefficient depends, in general, on both Reynolds and Mach numbers.

2.2 Stall

As anticipated in the previous section, the stall is a phenomena totally related to the maximum lift coefficient and it's always generated by the separation of the boundary layer, a thin viscous part of fluid, close to the airfoil surface.

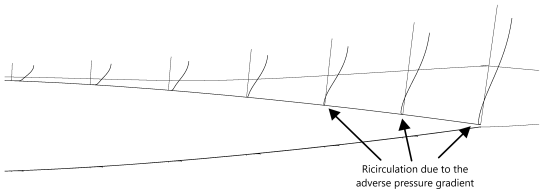

Figure 2.2. Boundary layer speed profiles on the NACA 0012 airfoil, showing the adverse pressure gradient effect which causes the separation

To better describe the stall mechanism, it is useful to look at a typical evolution of the pressure distribution over an airfoil in Figure 2.3. Starting from the frontal stagnation point with unit pressure coefficient, the flow accelerates due to the nose curvature: pressure coefficient decreases until the suction peak $C_{p\,min}$ reached at the point of maximum airfoil thickness. Passed the minimum peak, it follows a pressure recovery due to an adverse pressure gradient in the stream-wise direction (Figure 2.2). At very low inclinations, the aerodynamic shape and curvature of the airfoil attract the viscous flow, so it is easy to cope with the adverse gradient. However, increasing the angle of attack, the boundary layer separation starts due to the stronger adverse pressure gradient and it continues to grow, till a full stall is achieved (Figure 2.4). This separated boundary layer creates a turbulent wake, which quickly increases the drag.

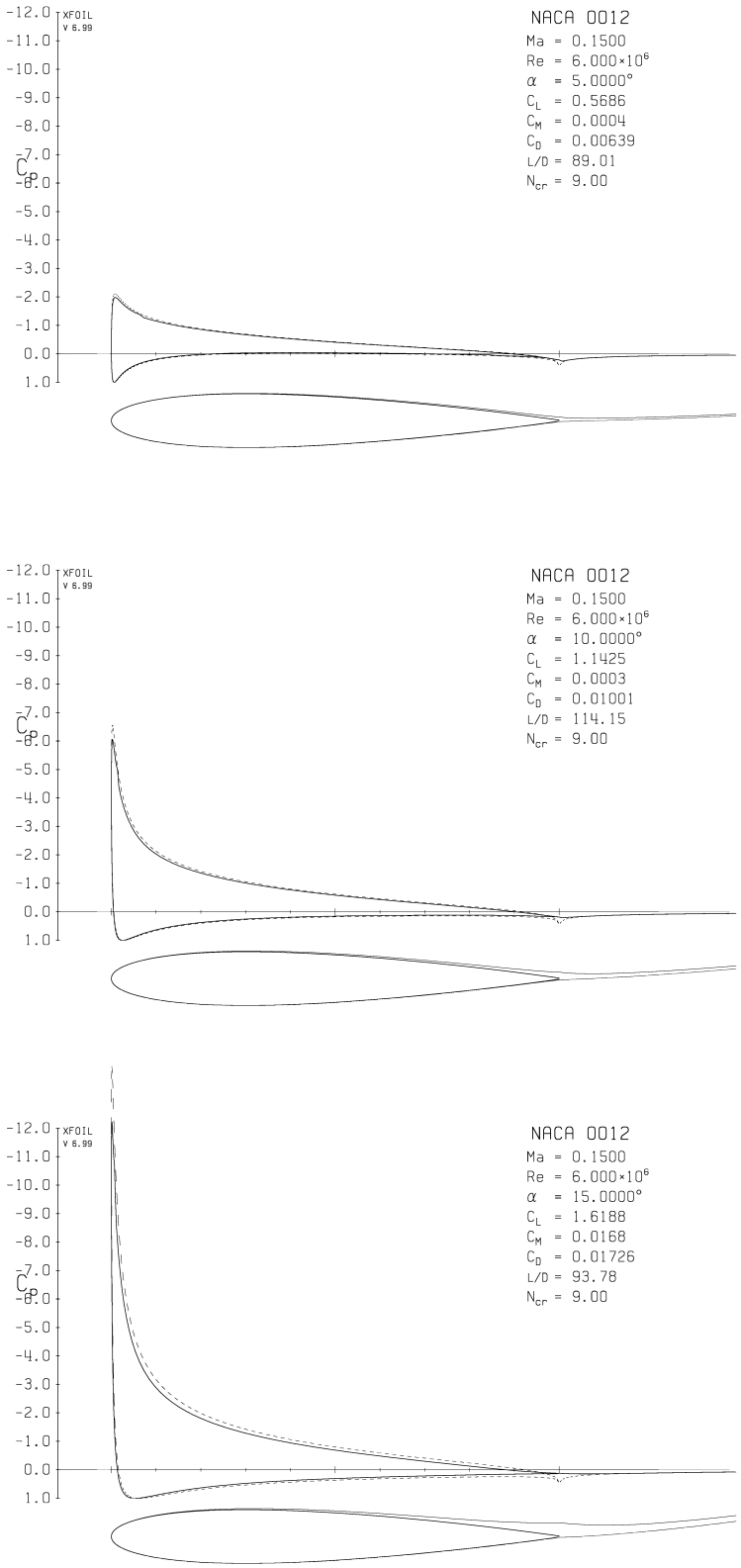

Figure 2.3. Typical evolution of the NACA0012 pressure distribution, respectively at $\alpha = 5°$, $\alpha = 10°$ and $\alpha = 15°$, computed by XFOIL

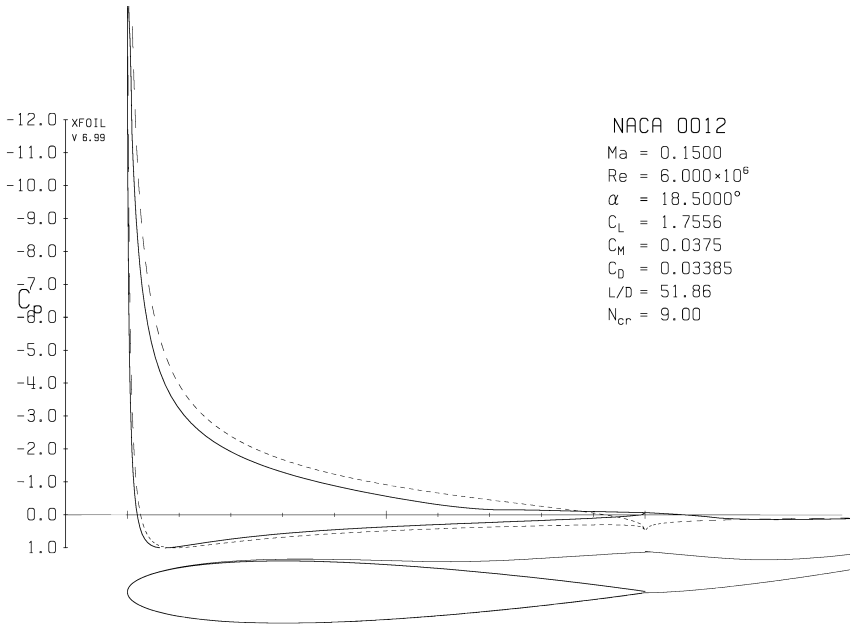

Figure 2.4. NACA0012 pressure distribution at the stall condition, i.e. $\alpha = 18.5° = \alpha_{stall}$, computed by XFOIL

The generation mechanism described above is, however, a bit different depending on the airfoil shape and thickness. In the McCullough and Gault research [7], the different types of airfoil stall are analysed and three main stall processes are identified.

The **trailing-edge stall** is the kind typical of the thick airfoil sections with $t/c > 0.15$. The growing rate of the lift coefficient decreases slowly near the stall, resulting in a well-rounded $C_L - \alpha$ curve, even after the maximum peak (Figure 2.6, case A). This behaviour is due to a steady movement of the turbulent boundary-layer separation point toward the leading edge, as depicted in Figure 2.5a.

The second type can be found on airfoils with a moderate thickness ($0.09 < t/c < 0.15$) and it is named **Leading-edge stall**. It can be a very dangerous stall, because it occurs suddenly, without any lift curve slope changes prior to the maximum lift coefficient (Figure 2.6, case B). The formation of this stall begins when the boundary layer is not able to overcome the high pressure gradient of the airfoil nose and a very small laminar separation bubble is created immediately after the suction peak, as represented in Figure 2.5b. Increasing the angle of attack, this bubble retreats, until it reaches the trailing edge and blows up, causing full chord flow separation and a very strong stall.

The so-called **thin-airfoil stall** is instead found on very thin airfoils ($t/c < 0.09$) or that have a sharp leading edge. The lift curve is often characterized by rounded peak. also in this case, a laminar separation bubble is created at the leading edge. At growing incidence, the re-attachment point moves towards the trailing edge (Figure 2.5c) and, when it coincides with the trailing edge, the flow is fully separated and the stall takes place.

Finally, it is possible to observe in some airfoils the **combination between trailing-edge and leading-edge stall**, presenting features of both types (Figure 2.5d). The behaviour of the lift curve near the peak depends on the dominance of stalling kind.

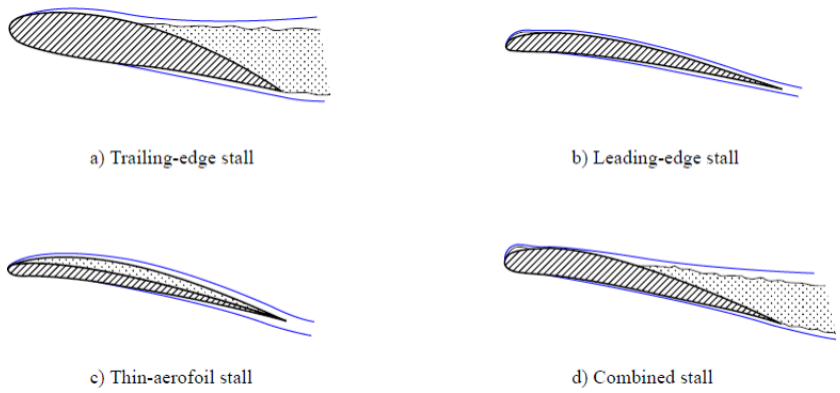

Figure 2.5. Flow behaviour the different stall types [5]

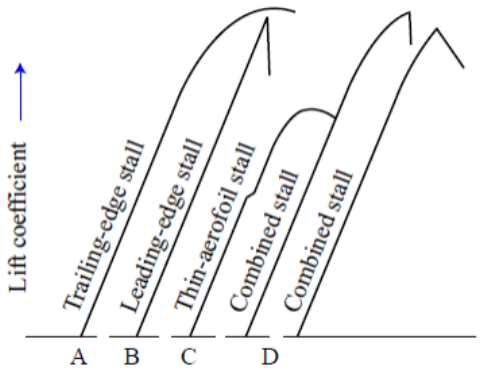

Figure 2.6. Typical lift coefficient polars for the different stall types [6]

Chapter 3

NACA airfoils

An airfoil is the cross-section of a wing, characterized by a particular shape, which produces the so-called aerodynamic force when moving in a fluid.

From the first decades after the Wright brothers' first flight, it was already understood the importance of studying new shapes able to generate a lift, keeping the drag low at the same time, and which could be geometrically described by parameterizations or analytic equations. This is the case of the famous **NACA airfoils** developed by the *National Advisory Committee for Aeronautics (NACA)* from the late 1920s till the 1940s. The peculiarity of the NACA airfoils is that their shapes are described in their own names, using a series of digits following the word "NACA": these numbers indicate the parameters which can be entered into equations to precisely generate the profile geometry and calculate its properties. In general, this parameterization employs analytic expressions to define the mean camber line and the thickness distribution along the chord. Depending on the number of digits, these airfoils are classified in families, each with different geometric and aerodynamic features: the best known and most widely used are the **4-digits series**, the **5-digit series** and the laminar family (or **6-series**).

3.1 4-digit Series

For a general airfoil NACA *mptt*, the four digits outline the profile as follows: the first number specifies the maximum camber m as chord percentage; the second one provides the distance p of the maximum camber point from the leading edge in tenths of chord; the last two digits describe the maximum thickness tt expressed as chord percentage [1, 2]. For example, the NACA 2412 airfoil presents a maximum camber of 2% located 40% (0.4 chords) from the leading edge, with a maximum thickness of 12% of the chord.

Starting from these three values, it is possible to calculate the coordinates of the entire profile using the following algorithm [1, 16]:

- Select an appropriate number of x coordinates along the chord, from 0 a c.

- Calculate the mean line coordinates with the following expressions:

$$y_c = \frac{m}{p^2}(2px - x^2)\,; \qquad x \in [0, p] \tag{3.1}$$

$$y_c = \frac{m}{(1-p)^2}[(1-2p) + 2px - x^2]\,; \qquad x \in [p, c] \tag{3.2}$$

- Calculate the thickness distribution along the chord above (+) and below (−) the mean line:

$$\pm y_t = \frac{tt}{200}(0.2969\sqrt{x} - 0.1260x - 0.3516x^2 + 0.2843x^3 - 0.1015x^4) \tag{3.3}$$

- Find the upper (x_U, y_U) and lower (x_L, y_L) surface coordinates:

$$\begin{aligned} x_U &= x - y_t \sin\theta \qquad & y_U &= y_c + y_t \cos\theta \\ x_L &= x + y_t \sin\theta \qquad & y_L &= y_c - y_t \cos\theta \end{aligned} \tag{3.4}$$

  where $\theta = \arctan(\frac{dy_c}{dx})$

From this equation set, the trailing edge thickness turns out to be non-null: that could lead to a relatively high drag coefficient. If, for computational reasons, the thickness needs to be zero, one coefficient of the relative equation has to be modified, such that their sum is zero, leading, however, to slight changes in the airfoil shape.

Thanks to this parameterization, a wide variety of airfoils can be described; however there are some limitations, which reduce their applicability. For example, it can be proved that, in NACA 4-digit series, the maximum thickness is always located at 30% of the chord.

In this report, eight airfoils of the 4-digits NACA family are studied (Figure 3.1), in order to represent a wide variability of characteristics, as symmetry, maximum thickness and camber line shape.

3.2 5-digit Series

The 5-digit NACA family adopts the same analytic expression of the previous series for the thickness distribution along the chord, but it uses a different and more complex expression for the chamber line. Having in general an advance curvature with respect to a 4-digit airfoil, both the lift and drag coefficients are improved.

Therefore, also the definition of the digits in the name is more intricate: its format is NACA *lpstt* and each digit is described as follows. The first number l represents 2/3 of the theoretical optimal lift coefficient at ideal angle of attack. The digit p stands for twice the x coordinate of the point of maximum camber in tenths, while s is a binary number indicating whether the camber is simple (0) or reflex (1); the reflexed camber line makes the negative trailing edge camber of the simple line to be

Table 3.1. Table of NACA 5-Digits values with simple camber line

Camber line	p	m	k_1
210	0.05	0.0580	361400
220	0.10	0.1260	51640
230	0.15	0.2025	15957
240	0.20	0.2900	6643
250	0.25	0.3910	3230

Table 3.2. Table of NACA 5-Digits values with reflexed camber line

Camber line	p	m	k_1	k_2/k_1
221	0.10	0.130	51.990	0.000764
231	0.15	0.217	15.793	0.00677
241	0.20	0.318	6.520	0.0303
251	0.25	0.441	3.191	0.1355

positively cambered: this results in a theoretical pitching moment of 0. The last two digits tt describe again the maximum thickness in chord percentage [1, 2]. Thus, the airfoil NACA 23012 is characterized by a design lift coefficient of 0.3, the point of maximum camber located at 15% chord, simple camber and maximum thickness of 12% of chord length.

Therefore, in this case, the coordinates of the airfoil can be obtained by following the point below [1, 16]:

- Select an appropriate number of x coordinates along the chord, from 0 a c.
- Calculate the chamber line with the following equations, obtaining the values of m, k_1 and k_2 from the Tables 3.1 and 3.2:

$$y_c = \begin{cases} \frac{k_1}{6}(x^3 - 3mx^2 + m^2(3-m)x) & \text{if } x \in [0, p] \\ \frac{k_1 m^3}{6}(1-x) & \text{if } x \in [p, c] \end{cases} \tag{3.5}$$

- Calculate the thickness distribution through the same 4-digit series equation 3.3.
- Determine the surface coordinates with relations 3.4.

The three most known 5-digits NACA airfoils are used in this thesis: the NACA 23012, the NACA 23021 and the NACA 23024 (Figure 3.2).

3.3 Laminar 6-digit Series

The 6-digit series were designed when propulsion began to improve flight speeds, in order to reduce the drag with respect to the previous 4 and 5-digit families. In these airfoils, the maximum thickness position is set back at about the 40% of the chord; this allows to move back the peak of the pressure coefficient (up to 60% of chord with respect of the 15% of a 4-digit NACA), so that the laminar boundary layer can be preserved as much as possible (from here the name "Laminar"). In this way, the friction coefficient is lower and the drag is reduced, but only for a small range of low angles of attack.

The airfoils of this family are described by six digits in the following order. The first is always a 6 and indicates the series. The second outlines the location of the minimum pressure area in tenths of the chord. Then, a subscript digit gives, in tenths, the range of lift coefficient above and below the design value, in which the low drag is maintained. Following a hyphen, the fourth number indicates the design lift coefficient in tenths. Finally, the last two digits describe, as usual, the maximum thickness as percent of chord [1].

For example, the NACA $63_1 - 212$ has the area of minimum pressure 30% of the chord back, maintains low drag for an interval of 0.1 above and below the lift coefficient of 0.2 and has a maximum thickness of 12% of the chord.

To design a laminar NACA airfoil it is necessary to solve an inverse problem by means of conformal transformations, relating the flow about an arbitrary airfoil to that of a circle [3].

In Figure 3.3, the laminar airfoils used in this report are depicted.

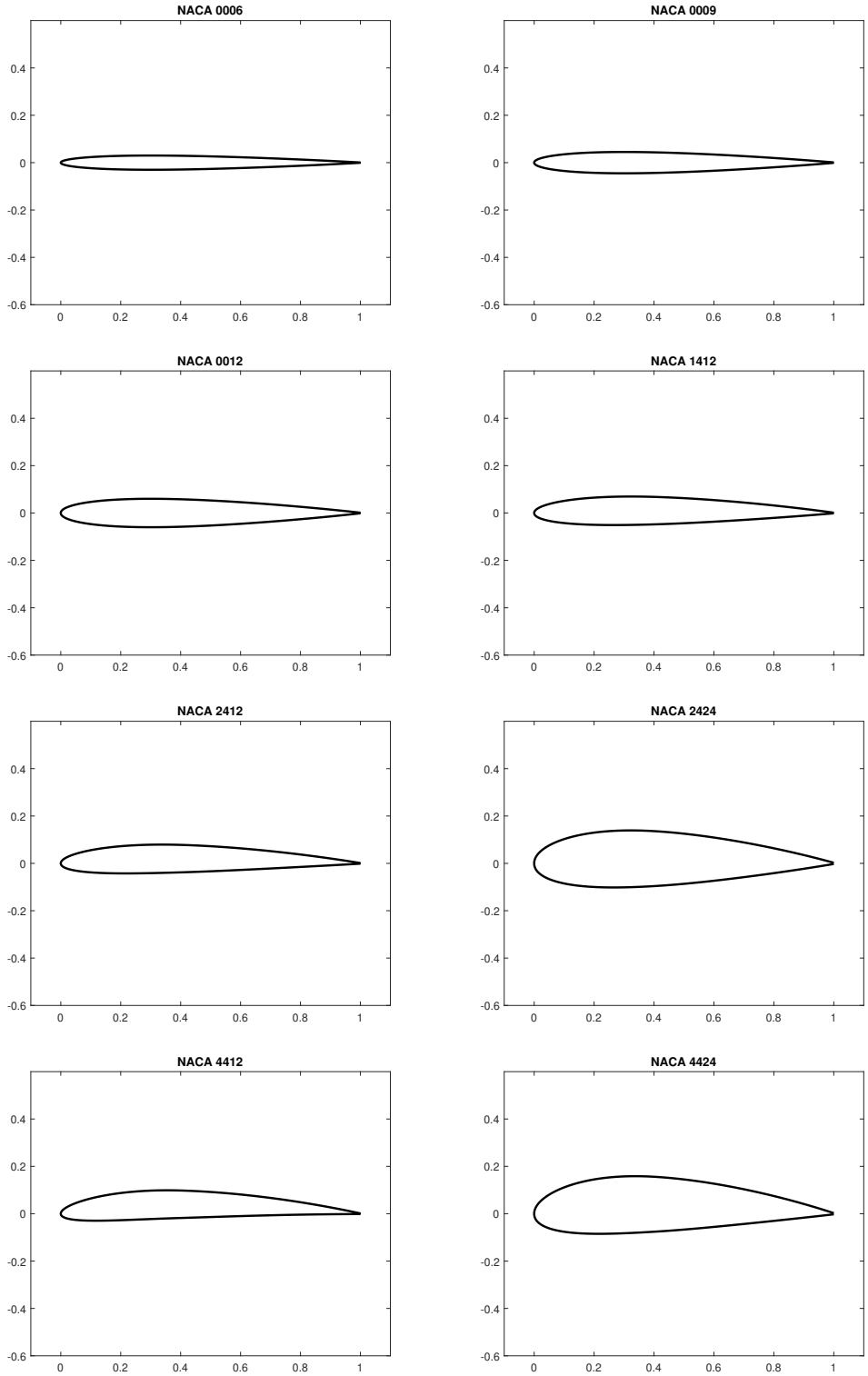

Figure 3.1. NACA 4-digits airfoils

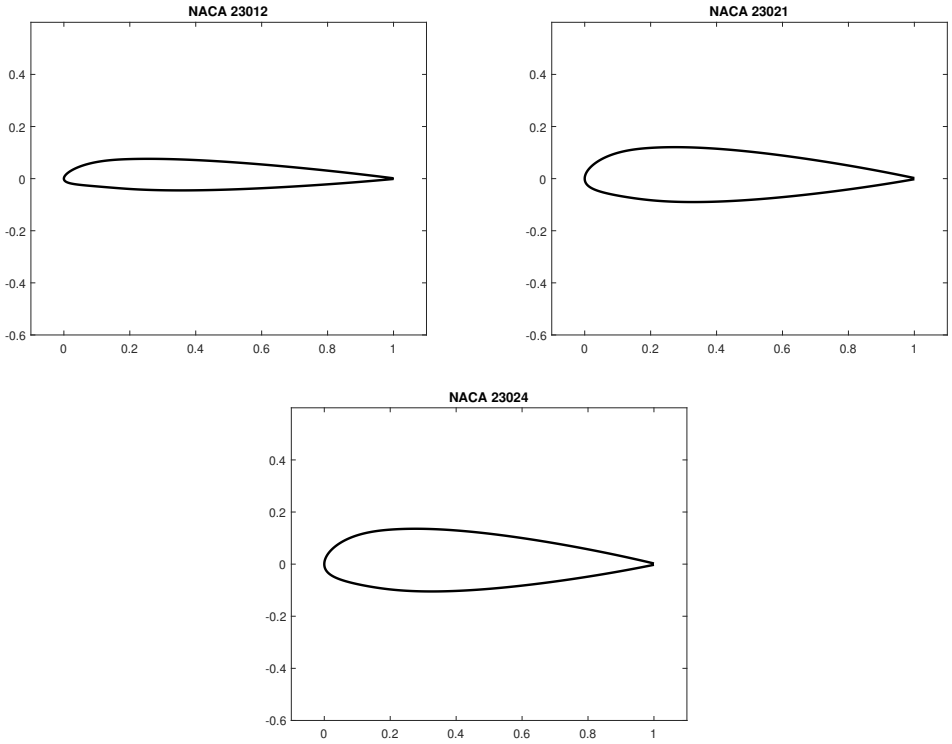

Figure 3.2. NACA 5-digits airfoils

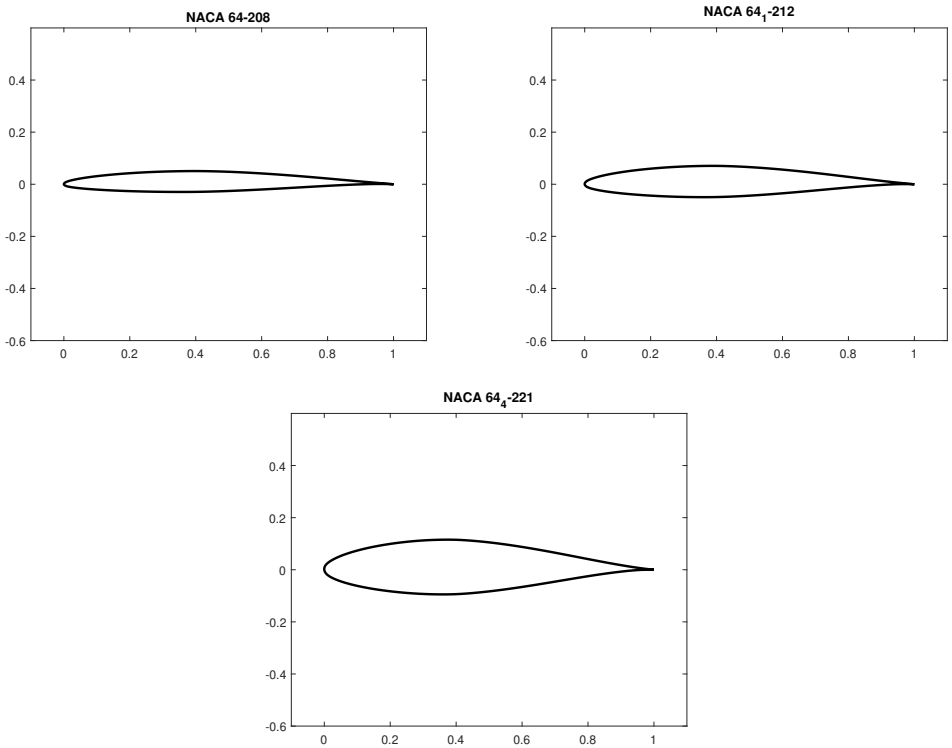

Figure 3.3. NACA 6-digits airfoils

Chapter 4

XFOIL

XFOIL is a program, realized by the MIT engineer Mark Drela, which allows to solve linear fluid-dynamics problems about subsonic flows around 2D airfoils. Using a combination of a panel method based on kinetic potential and a boundary layer calculation, it computes the aerodynamics coefficients, also allowing the introduction of viscosity. Its basic functioning is described in the article *"XFOIL: An Analysis and Design System for Low Reynolds Number Airfoils"* by Drela [4], to which this chapter refers.

The panel method is similar to the Hess-Smith method, considering a vorticity and source distribution for each panel, but it's more accurate, since it's based on the streamfunction which ensures to impose the boundary conditions on the airfoil in a more robust way: it's required not only that the perpendicular velocity is null on the boundary control points, but also that every panel belongs to a streamline and thus it isn't crosses by the fluid.

The viscous analysis for the boundary layer employs the integral method with the Von Karman equation and empiric experimental relations, being quite precise on the estimate of turbulent transition.

Through the Karman-Tsien correction, the validity field of the program is extended with the compressible subsonic conditions.

Due its low computational cost and its quite reliable results, Xfoil is classified as a *medium-fidelity* technique.

The code contains a useful database of NACA airfoils, but it is also possible to upload different airfoils with text files and to modify their shape depending on user requirements.

4.1 Inviscid Formulation

As in any panel method, Xfoil discretized both the airfoil contour and the wake into flat panels, each one delimited by two nodes, N if belonging to the airfoil or N_w if related to the wake. Each airfoil panel is characterized by a linear vorticity

distribution on the node values γ_i $(1 \leq i \leq N)$. Each airfoil and wake panel also has a constant source strength σ_j $(1 \leq j \leq N + N_{w-1})$, which will be related to viscous layer quantities. In the case of trailing edge with finite thickness, the intensities σ_{TE} and γ_{TE} have to be placed across the trailing edge gap and they have to be described as:

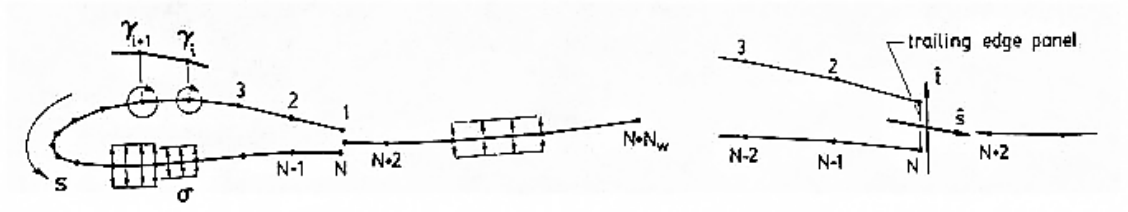

Figure 4.1. Airfoil and wake paneling with vorticity and source distributions, with trailing edge details

$$\sigma_{TE} = \frac{1}{2}(\gamma_1 - \gamma_N)|\hat{s} \times \hat{t}| \qquad \gamma_{TE} = \frac{1}{2}(\gamma_1 - \gamma_N)|\hat{s} \cdot \hat{t}| \tag{4.1}$$

where s is the unit vector bisecting the trailing edge angle and t is the unit vector along the trailing edge panel as shown in Figure 4.1.

Hence, the flowfield around the airfoil is constructed by the superimposition of a freestream flow, a vortex sheet γ and a source sheet σ, such that the streamfunction is

$$\Psi(x,y) = u_\infty y - v_\infty x + \frac{1}{2\pi}\int \gamma(s) \ln r(s;x,y)\,\mathrm{d}s + \frac{1}{2\pi}\int \sigma(s)\theta(s;x,y)\,\mathrm{d}s \tag{4.2}$$

$$\boldsymbol{U} = \begin{Bmatrix} u_\infty \\ v_\infty \end{Bmatrix} = \begin{Bmatrix} q_\infty \cos\alpha \\ q_\infty \end{Bmatrix} \tag{4.3}$$

where s is the coordinate along vortices and sources, r is the magnitude of the vector between s and the field point (x, y) and θ is the vector angle.

Applying the discretization

$$\begin{aligned} \Psi(x,y) = u_\infty y - v_\infty x &+ \frac{1}{4\pi}\sum_{j=1}^{N+N_w-1} \Psi_j^\sigma(x,y) 2\sigma_j + \\ &+ \frac{1}{4\pi}\sum_{j=1}^{N-1} \Psi_j^{\gamma+}(x,y)(\gamma_{j+1} + \gamma_j) + \Psi_j^{\gamma-}(x,y)(\gamma_{j+1} - \gamma_j) \\ &+ \frac{1}{4\pi}(\Psi_N^\sigma(x,y)|\hat{s} \times \hat{t}| + \Psi_N^{\gamma+}(x,y)|\hat{s} \cdot \hat{t}|)(\gamma_1 - \gamma_N)\ . \end{aligned} \tag{4.4}$$

Defining the geometry of each panel and assuming that the streamfunction is equal to a constant value Ψ_0 at each airfoil node, the following linear system can be

derived.

$$\sum_{j=1}^{N} a_{ij}\gamma_j - \Psi_0 = -u_\infty y_i + v_\infty x_i - \sum_{j=1}^{N+N_w-1} b_{ij}\sigma_j \; ; \qquad 1 \leq i \leq N \tag{4.5}$$

Then, adding the Kutta condition

$$\gamma_1 + \gamma_N = 0 \tag{4.6}$$

results a linear system whit $N+1$ equations and $N+1$ unknowns (the vortex strength γ_i and the constant Ψ_0).

In the case of a sharp trailing edge, where the nodes 1 and N coincide, the corresponding equations in the system 4.5 are identical and hence the singular system cannot be solved for γ_i. In order to solve the problem, the *N-th* equation is discarded and replaced by an extrapolation of the mean γ on the trailing edge

$$(\gamma_3 - 2\gamma_2 + \gamma_1) - (\gamma_{N-2} 2\gamma_{N-1} + \gamma_N) = 0 \; . \tag{4.7}$$

4.2 Viscous Formulation

The fundamental equations employed for the viscous formulation are the standard compressible integral momentum and kinetic energy shape parameter equations

$$\frac{\mathrm{d}\theta}{\mathrm{d}\xi} + \left(2 + H - M_e^2\right) \frac{\theta}{u_e} \frac{\mathrm{d}u_e}{\mathrm{d}\xi} = \frac{C_f}{2} \tag{4.8}$$

$$\theta \frac{\mathrm{d}H^*}{\mathrm{d}\xi} + (2H^* * + H^*(1-H)) \frac{\theta}{u_e} \frac{\mathrm{d}u_e}{\mathrm{d}\xi} = 2C_D - H^* \frac{C_f}{2} \tag{4.9}$$

where ξ is the streamwise coordinate.

Moreover, in order to consider deviations of the outer layer dissipation coefficient C_D from the local equilibrium value, a rate equation for the maximum shear stress coefficient C_τ is used

$$\frac{\delta}{C_\tau} \frac{\mathrm{d}C_\tau}{\mathrm{d}\xi} = 5.6(C_{\tau_{EQ}}^{1/2}) + 2\delta \left\{ \frac{4}{3\delta^*} \left[\frac{C_f}{2} - \left(\frac{H_k - 1}{6.7 H_k} \right)^2 \right] - \frac{1}{u_e} \frac{\mathrm{d}u_e}{\mathrm{d}\xi} \right\} \; . \tag{4.10}$$

In laminar regions, the latter equation 4.10 is replaced by a different relation which describes the growth of the amplitude $\tilde{n}$ of the most amplified Tollimen-Schlichting wave

$$\frac{\mathrm{d}\tilde{n}}{\mathrm{d}\xi} = \frac{\mathrm{d}\tilde{n}}{\mathrm{d}Re_\theta}(H_k) \frac{\mathrm{d}Re_\theta}{\mathrm{d}\xi}(H_k, \theta) \; . \tag{4.11}$$

Therefore, the principal variables in the boundary layer equations are θ, δ^* and C_τ or $\tilde{n}$ in laminar regions, and they are located at the panel nodes. In addition, u_e is present as an external unknown, related to the global solution through the inviscid outer flow. The other auxiliary variables are expressed in terms of the principal ones, such that the integral boundary layer equations 4.8, 4.9 and 4.10 can be closed.

$$H_k = H_k(H, M_e) \qquad H^* = H^*(H_k, M_e, Re_\theta) \qquad H^{**} = H^{**}(H_k, M_e) \qquad U_S = U_S(H^*, H, H_k)$$
$$C_{\tau_{EQ}} = C_{\tau_{EQ}}(H^*, H, H_k, U_S) \qquad C_f = C_f(H_k, M_e, Re_\theta) \qquad C_D = \frac{C_f}{2} U_S + C_\tau (1 - U_S) \; . \tag{4.12}$$

The wake is considered as one viscous layer where a single θ and δ^* is present at each wake station, with the following initial conditions at the airfoil trailing edge

$$\theta_{wake} = \theta_{upper} + \theta_{lower} \qquad \delta^*_{wake} = \delta^*_{upper} + \delta^*_{lower} + h_{TE} \; . \tag{4.13}$$

The wake shear coefficient is instead taken as the θ-weighted average of upper and lower surface values:

$$C_{\tau\ wake} = \frac{C_{\tau\ upper}\theta_{upper} + C_{\tau\ lower}\theta_{lower}}{\theta_{upper} + \theta_{lower}} \; . \tag{4.14}$$

The governing equations 4.8, 4.9, 4.10,4.11 are discretized using two-point central differences, thus three coupled nonlinear equations are associated with each panel, and they are solved by the following procedure.

4.3 Inviscid-Viscous Coupling

While for the airfoil surface, since the internal flow is stagnant, u_e is simply equal to the vorticity γ on the suction side and to $-\gamma$ on the pressure side, for the wake it is necessary to relate u_e to the freestream and to a sum of all vortices and sources of the airfoil:

$$u_{e_i} = \pm\gamma_i \qquad \text{if} \qquad 1 \le i \le N$$

$$\begin{aligned} u_{e_i} &= \nabla\Psi \cdot \hat{n} \\ &= u_\infty \hat{n}_y - v_\infty \hat{n}_x + \sum_{j=1}^{N} c^\gamma_{ij}\gamma_j + \sum_{j=1}^{N+N_w-1} c^\sigma_{ij}\sigma_j \qquad \text{if} \qquad N+1 \le i \le N+N_w \; . \end{aligned} \tag{4.15}$$

The viscous layer contribute is described by the wall transpiration concept: the source intensity is equal to the local gradient of the mass defect m.

$$m = u_e \delta^* \qquad , \qquad \sigma_i = \left.\frac{\mathrm{d}m}{\mathrm{d}\xi}\right|_i = \pm\frac{m_{i+1} - m_i}{s_{i+1} - s_i} \tag{4.16}$$

Thus, the expression 4.15 can be reformulated as the sum of the inviscid speed, given by the free stream velocity and the vortices, and the viscous speed, described by the mass deflection.

$$u_{e_i} = u_{INVISCID_i} + \sum_{j=1}^{N+N_w-1} d_{ij} m_j \qquad 1 \leq i \leq N + N_w \tag{4.17}$$

4.4 Solution

The boundary layer equations 4.8, 4.9, 4.10 ,4.11 can be now closed by the explicit expression 4.17 for u_{e_i}, generating a non-linear elliptic (due to the global mass influence) system, which is solved by a full Newton method.

$$\begin{bmatrix} & & \\ & J_{ij} & \\ & & \end{bmatrix} \begin{Bmatrix} \delta\theta_j \\ \delta m_j \\ \delta\tilde{n}_j \ , \ \delta C_{\tau j} \end{Bmatrix} = \begin{Bmatrix} -R_i \\ \\ \end{Bmatrix} \qquad 1 \leq i \leq N + N_w \tag{4.18}$$

where $\delta\theta$, δm and $\delta\tilde{n}$ (or δC_τ depending on whether the i-th station is laminar or turbulent) are the Newton variables.

Chosen a proper initial guess x_0 and rewriting the system as $F(x, r) = 0$, the iterative solution is

$$x_{N+1} = x_N - J_F(x_N, r)^{-1} F(x_N, r) \qquad (J_F \text{ is the Jacobian matrix of } F) \tag{4.19}$$

4.5 Karman-Tsien Compressibility Correction

For the compressible flow, Xfoil approximates the compressible speed q and the pressure coefficient C_p starting from the incompressible values

$$C_p = \frac{C_{p\,INC}}{\beta + \lambda(1+\beta)C_{p\,INC}/2} \qquad q = \frac{q_{INC}(1+\lambda}{1 - \lambda(q_{INC}/q_\infty)^2} \tag{4.20}$$

where $\beta = \sqrt{1 - M_\infty^2}$ and $\lambda = M_\infty^2/(1+\beta)^2$.

Chapter 5

Valarezo-Chin Method

Relying on the Smith report [11] and noticing a recurrence on wind tunnel tests, the engineers and AIAA members Valarezo and Chin reported in 1994 their own *"Method for the Prediction of Wing Maximum Lift"* [12].

The Smith report theorizes the maximum lift expectation on clean airfoils from two empirical observations, both based on the pressure coefficient peak; however, this criterion has an important inaccuracy: it doesn't depend on Reynolds and Mach numbers, parameters known to have a key influence on maximum lift. Valarezo and Chin filled these lack finding an interesting correlation on wind-tunnel data at maximum lift conditions.

According to their so-called **Pressure difference rule**, at a given Reynolds and Mach number combination, there exists a certain pressure difference between the suction peak and trailing edge at the maximum lift condition.

$$\text{If} \qquad |\Delta C_p| = |C_{p\,PEAK} - C_{p\,TE}| = \Delta C_p^{\text{V-C}}(Re, M) \qquad \Longrightarrow \qquad C_L = C_{L\,MAX} \tag{5.1}$$

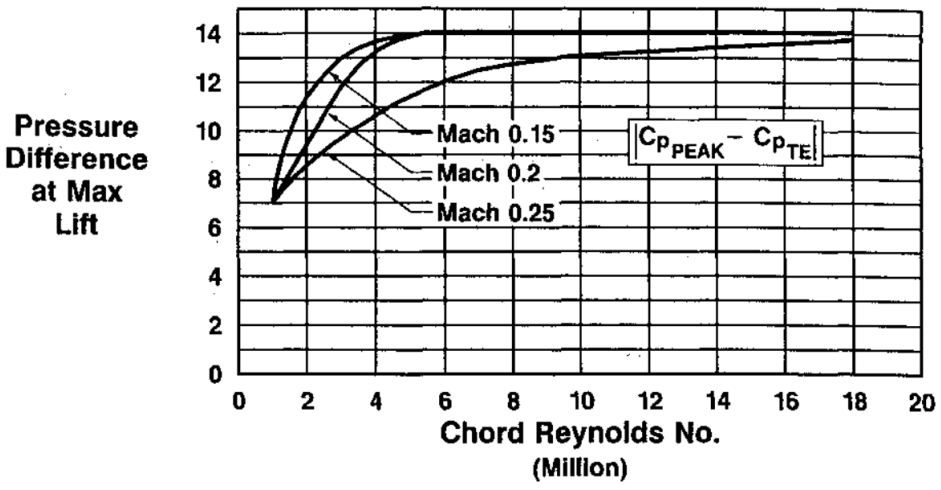

Figure 5.1. Pressure difference rule for maximum lift [12]

This pressure difference value that indicates when the maximum lift is reached, is reported on the plot of Figure 5.1. The criterion is valid also for multielement airfoils, applying the rule to each of the elements.

From the Figure 5.1, it's simple to note the strong dependency of the Pressure difference rule on Reynolds number for low Reynolds numbers. For $M < 0.2$, this dependency is lost when $Re > 6 \times 10^6$ and this can be explained by the fact that, at growing Re, the viscous effect on the airfoil decreases and the boundary layer gets thinner. Instead, when $M > 0.2$, on an airfoil at maximum lift condition appears a supersonic bubble on the zone of minimum suction peak: a shock is generated and a boundary layer separation occurs. This viscous phenomenon is strongly dependent on Re.

According to Valarezo and Chin, the method is also applicable to three dimensional wings, thanks to the following procedure:

- The wing is divided in several wing stations; at each station i, the effective Reynolds and Mach numbers are computed:

$$V_{eff,i} = \frac{V_{\perp i}}{\cos \alpha_i} \qquad M_{eff,i} = \frac{V_{eff,i}}{a} \qquad Re_{eff,i} = Re_\infty \frac{V_{eff_i}}{V_\infty} \frac{c_{\perp i}}{c_i} \tag{5.2}$$

- The critical pressure difference distribution over the wing span is constructed using the effective Reynolds and Mach numbers in conjunction with the plot 5.1.

- Using a low computational method, as a surface panel method, the chordwise pressure differences over the wing span is computed at increasing angles of attack.

- The previous step is repeated until the curve produced gets close to the one obtained at the second step within an user-specified error margin (Figure 5.2): the C_L at which this occurs, is the $C_{L\,MAX}$.

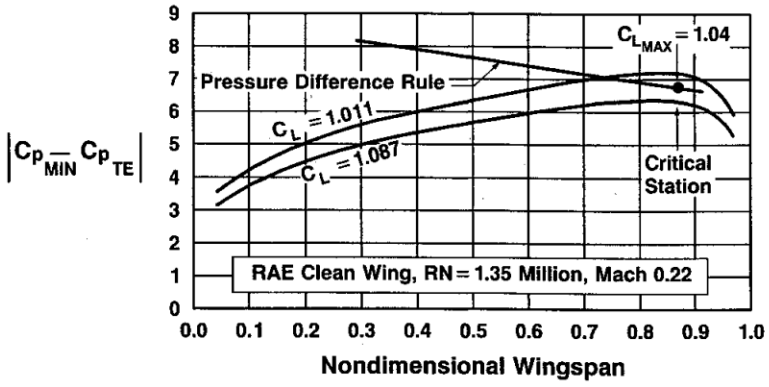

Figure 5.2. Example of pressure difference rule usage on a 3D wing [12]

Chapter 6

Verification of the method

This chapter describes step by step the process followed in order to verify the proper functioning of the Valarezo-Chin method. The checking is performed with the employment of the medium fidelity program XFOIL, described in the Chapter 4.

After getting the computational data, the post-processing operations are carried out with MATLAB and the results are compared with experimental data from the *"Theory of Wing Sections - Including a summary of airfoil data"* [1] and the *"Report No. 824"* [2] by I. H. Abbott and A. E. Von Doenhoff. In this papers, the geometric and aerodynamic characteristics of a large number of NACA airfoils are listed: the maximum lift coefficients $C_{L\,max}$ of all of them are depicted in Figure 6.1, which also shows the variability of this parameter in relation to the airfoil shape. The aerodynamics characteristics were produced on a two-dimensional low-turbulence pressure wind tunnel, with tests made over a range of Reynolds numbers from 3 to 9 million and at Mach numbers of about 0.17, and the data are reported in the form of plot: for this reason, it was deemed necessary to digitize the graphs of interest with the online tool *WebPlotDigitizer* [15], thus obtaining a digitized database of the airfoils analyzed in this thesis.

As mentioned in Chapter 3, from this long list, only a few airfoils of each NACA family are studied, but chosen so that a wide selection of features, which may affect the stall, are represented. In particular, airfoils from each of the three main families, both symmetric and with curved camber-line, are analyzed. Three different thickness are considered, such that thin (6/8% of chord), medium-thickness (12% of chord) and thick (24% of chord) airfoils are present.

Since the computational results have to be compared with the Abbott and Von Doenhoff's experimental data, all the XFOIL simulations are run at $M = 0.15$: in such a way the compressibility effects and all the issues arising from them can be neglected. Among the Reynolds numbers proposed by Abbott and Von Doenhoff, the choice falls on $Re = 6 \times 10^6$, in order that the pressure difference rule 5.1 is independent from the Reynolds variations.

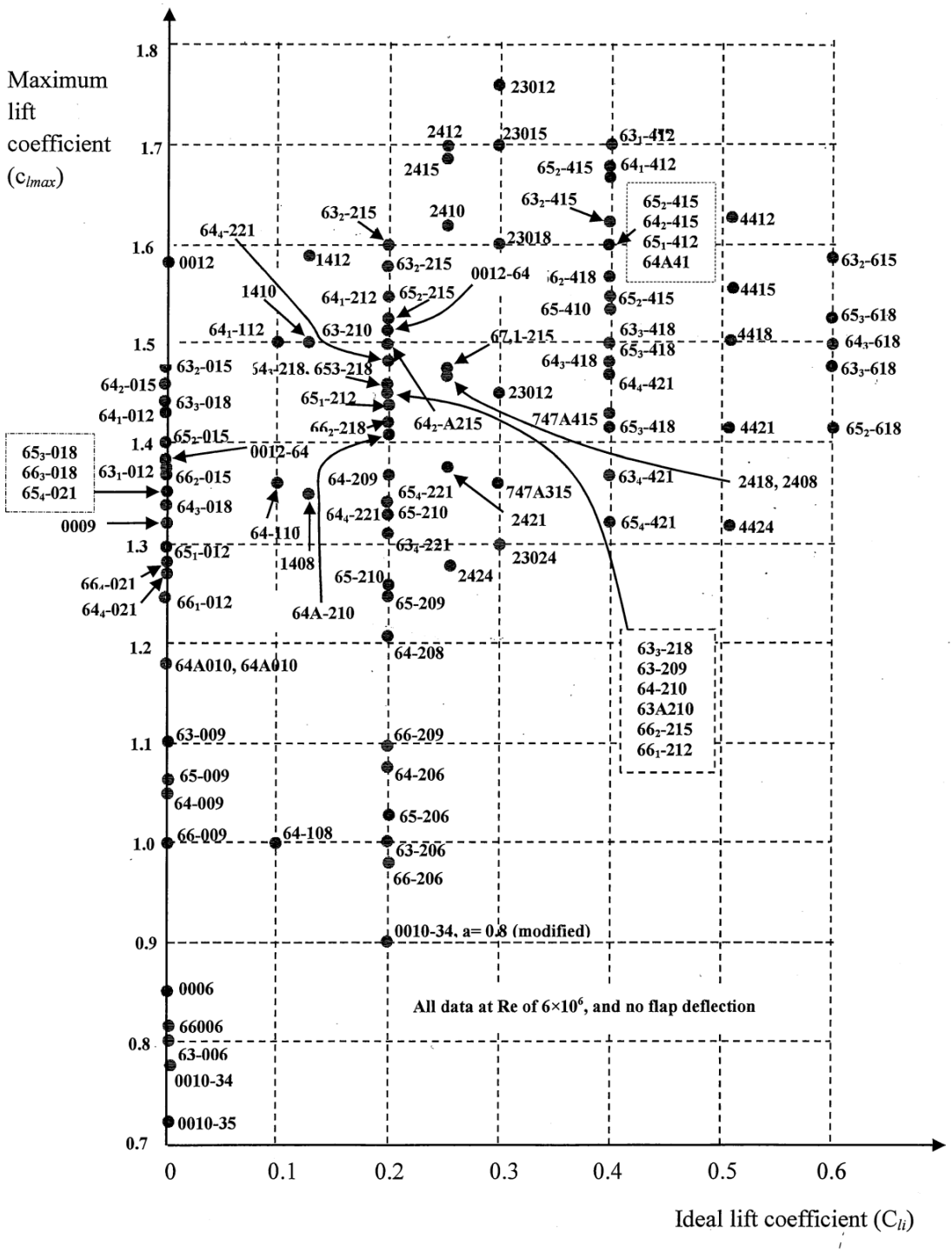

Figure 6.1. Collection of the maximum lift coefficients of all the airfoils included in Abbott and Von Doenhoff's report [2], in relation to their ideal lift coefficients, i.e. the C_L for which the airfoil is designed.

6.1 Variability of XFOIL results

Before considering the the Valarezo-Chin method, it seems necessary to conduct a research on the results variability of XFOIL in calculating the maximum lift coefficient. To carry out this first analysis, the NACA 0012 airfoil is taken into account as case study.

Based on the parameters which XFOIL allows you to modify before the computation, the effects of three variable variation are analyzed: the number n_{pan} of panels on the airfoil surface, the angle of attack increment step $\Delta\alpha$ and the N_{crit} coefficient of the e^N method for transition prediction. The results and the choices arising from this parametric study with the NACA 0012 will be applied also to the other airfoils.

The number of panels is varied between 100 and 450 with steps of 50. With a low n_{pan} value a coarse airfoil is obtained, while an higher number of panel gives a very refined paneling and it leads to a computationally expensive simulation. The plots in Figure 6.2 show that this parameter does not affect the computation of the maximum lift coefficient: the $C_{L\,max}$ value oscillates within a range of about 0.015, i.e with an uncertainty of 0.01%, while the α_{stall} fluctuations are over an interval of 0.4°, i.e. of 0.02%. Since these variations seem to have no dependence with the n_{pan} increase and since the panel number suggested by XFOIL is 160, it is decided to use $n_{pan} = 300$, because it is a good compromise between a smooth airfoil and a low computational cost.

This first analysis might seem the most critical when changing the airfoil, since the paneling and the inclination of panels depend on the airfoil shape and they can affect the computation; however, the same evaluation was conducted on different profiles, showing the same results and coming to the same conclusions.

The second parameterization is done with the angle of attack increment of values between 0.01° and 2°. Apart from the increment steps of 2° and 1°, which draw curves too fragmented and are not able to identify the right stall, all the others detect the same $C_{L\,max}$ with smooth and well-defined lines, as depicted in Figure 6.3. Also in this case, in order to avoid a relatively high computational cost, the middle parameter $\Delta\alpha = 0.1°$ is taken as reference.

In order to predict the position of the transition point, the e^N *method* is implemented in XFOIL. This is an approach based on analysing the stability of the boundary layer: superimposing small disturbances in boundary layer, if one of them causes an unstable solution in the Navier-Stokes equations, hence it could lead to a transition point. Downstream the first point where this happens, the amplification of the disturbances grows rapidly. With the method e^N, the evolution of disturbance amplification in the flow is evaluated along the surface, trying to get a critical value for N that indicates the transition. The typical value of $N_{crit} = 9$ is found experimentally, however it can vary from 3 to 13, respectively for dirty wind-tunnel flows or atmospheric turbulence and for clean wind tunnels flows [13].

As can be noticed in Figure 6.4, also the N_{crit} value doesn't affect the stall

computation: as recommended by XFOIL, the typical value is left as reference.

6.2 Comparison with experimental data

After selecting the reference parameters for the XFOIL computations, the C_L-α curves are thus obtained for all the NACA airfoils considered in this thesis and they are compared to the experimental ones from the Abbott and Von Doenhoff's reports [1, 2] (Figures from 6.5 to 6.16).

In general, XFOIL is often capable to best simulate the curve in its central part for angles between -10° and 10° approximately. However, when approaching the stall condition, it tends to overestimate the values of both $C_{L\,max}$ and α_{stall}. Thinking about a full aircraft project, this is the worst prediction for the stall: since it is a state to be avoided due its dangerousness, a computational forecast, which happens after the real condition, makes the project not work.

Analyzing the airfoils in more detail (Table 6.1), it is noted that, for the NACA 4-digits and 5-digits families, the best represented stalls are the ones of the airfoils with both a mid thickness (12% of the chord) and null or low camber, like the NACA 0012 (Figure 6.7), the NACA 1412 (Figure 6.8), the NACA 2412 (Figure 6.9) and the NACA 23012 (Figure 6.13). Here, the error on the $C_{L\,max}$ is under the 10% and the α_{stall} differs by no more than 2° from the experimental one.

Table 6.1. Comparison between Abbott and Von Doenhoff's experimental data and XFOIL results for the stall

NACA	α_{stall}^{EXP}	$C_{L\,max}^{EXP}$	α_{stall}^{XFOIL}	$C_{L\,max}^{XFOIL}$
0006	9.1°	0.84	11.4°	1.1931
0009	13.3°	1.32	16.5°	1.6403
0012	16.5°	1.58	18.5°	1.7502
1412	14.7°	1.57	18.3°	1.8043
2412	17.3°	1.67	18.6°	1.8489
2424	15.6°	1.28	19.3°	1.6932
4412	14.3°	1.63	17.7°	1.9137
4424	14.2°	1.32	17.6°	1.7960
23012	17.3°	1.73	17.9°	1.8110
23021	15.3°	1.48	20°	1.8890
23024	15.1°	1.30	20.5°	1.8435
64-208	10.1°	1.20	13.1°	1.5148
64_1-212	15.2°	1.56	18.2°	1.7480
64_4-221	19.8°	1.34	23°	1.6012

The increase of the thickness and/or the camber implies an early split of the computed C_L-α curve frome the Abbott and Von Doenhoff's one: both the errors of lift coefficient and angle grow significantly for the NACA 2424 (Figure 6.10), the

NACA 4412 (Figure 6.11), the NACA 4412 (Figure 6.12) and the NACA 23024 (Figure 6.14). Instead, for the thinner airfoils on Figures 6.5 and 6.6, the experimental $C_{L\,max}$ stands almost on the curve obtained by XFOIL, even though still in advance with respect of the computed stall, generating anyway a increase of the errors.

As depicted in Figures 6.15, 6.16 and 6.17, the characteristics of the lift coefficient plot and the dependencies on thickness and camber are similar also for the laminar NACA airfoils, but the stall prediction is incorrect ever for the one with the 12% thickness.

6.3 Validity check of the Valarezo-Chin method

Having established that XFOIL computes higher stall characteristics than the experimental ones, it is still used in order to try to validate the criterion of Valarezo and Chin (described in Chapter 5), but with all due considerations and cares.

The first reasoning made is to check whether the pressure coefficient difference $|\Delta C_p|$ computed/found with XFOIL at the experimental stall angle α_{stall}^{EXP} is equal to the critical value theorized by Valarezo and Chin on the *pressure difference rule*, which, for $Re = 6 \times 10^6$ and $M = 0.15$, is $\Delta C_p^{\text{V-C}}(Re, M) = 14$, as shown in Figure 6.19.

Table 6.2. C_p difference between suction peak and trailing edge for the Abbott and Von Doenhoff's stall angle, computed by XFOIL

NACA	α_{stall}^{EXP}	$C_{L\,max}^{EXP}$	$\lvert\Delta C_p\rvert_{INV}$	$\lvert\Delta C_p\rvert_{VISC}$
0006	9.1°	0.84	18.0205	15.7385
0009	13.3°	1.32	16.9107	16.2482
0012	16.5°	1.58	15.5537	14.0150
1412	14.7°	1.57	13.6184	11.0952
2412	17.3°	1.67	17.3955	12.4998
2424	15.6°	1.28	6.4779	4.2400
4412	14.3°	1.63	11.9005	8.4312
4424	14.2°	1.32	5.2321	3.5289
23012	17.3°	1.73	15.1981	10.9622
23021	15.3°	1.48	6.1046	4.6801
23024	15.1°	1.30	5.9276	4.4237
64-208	10.1°	1.20	17.2301	16.6110
64_1-212	15.2°	1.56	21.5199	16.1563
64_4-221	19.8°	1.34	16.0421	8.6731

The computations are done for every airfoil at both inviscid and viscous condition, obtaining the data in the Table 6.2. At first glance, the results are very irregular and especially different from the critical value. First of all, it has to be remind that, at the experimental stall angle, XFOIL generates a lift coefficient relatively higher than

the correct one: this causes certainly an error on the pressure coefficient distribution. However, some features and recurrences, depending on the airfoils characteristics, can be found.

Looking at the inviscid column, the $|\Delta C_p|$ values closer to 14 belong to the airfoils with 12% thickness and zero or small camber, i.e. the ones of whom XFOIL best represent the lift coefficient. The thinner airfoils have an higher pressure coefficient difference, around 17 and 18, while for the thicker ones a very lower value near to 6 is found, due to $|\Delta C_p|$ peak reduced by the wide curvature of the airfoil nose. The laminar NACA seem, instead, not to follow this rule.

The $|\Delta C_p|_{VISC}$ values are, instead, lower, but they generally keep the same behaviour based on the airfoil characteristics: a value about 11-14 for airfoils with mid thickness, it grows by lowering the thickness and decreases by raising the thickness or the camber.

To see if there is a rule with a more constant pressure coefficient difference and without the dependence on the error between computational and experimental data, the same steps and operations are repeated for the α_{stall} of XFOIL (Table 6.3). The same conclusions and considerations, explained above, are achieved, but with greater values.

Table 6.3. C_p difference between suction peak and trailing edge for the XFOIL stall conditions, computed by XFOIL

NACA	α_{stall}^{XFOIL}	$C_{L\,max}^{XFOIL}$	$\lvert\Delta C_p\rvert_{INV}$	$\lvert\Delta C_p\rvert_{VISC}$
0006	11.4°	1.1931	29.3713	21.9977
0009	16.5°	1.6403	25.1457	22.3759
0012	18.5°	1.7502	19.5571	15.9713
1412	18.3°	1.8043	21.0389	14.7265
2412	18.6°	1.8489	21.2429	13.8861
2424	19.3°	1.6932	8.7721	4.9887
4412	17.7°	1.9137	18.4054	11.2439
4424	17.6°	1.7960	6.9183	4.1037
23012	17.9°	1.8110	16.4938	11.4224
23021	20°	1.8890	9.1459	5.8783
23024	20.5°	1.8435	8.5336	5.3906
64-208	13.1°	1.5148	29.2473	26.7949
64_1-212	18.2°	1.7480	31.6750	20.5795
64_4-221	23°	1.6012	21.1172	10.0357

As a last analysis, it is considered to be interesting to observe the $|\Delta C_p|$, computed at the α^{XFOIL} for which it happens that $C_L^{XFOIL} = C_{L\,max}^{EXP}$. The Table 6.4 shows that, in this case, the symmetric airfoils present the values nearest to 14. A slight camber, as the one of NACA 1412, 2412 and 23012, generates a reduction to about 11, while the the thicker airfoils have a $|\Delta C_p|$ around 4, as usual.

Table 6.4. C_p difference between suction peak and trailing edge corresponding to the Abbott and Von Doenhoff's maximum lift coefficient, computed by XFOIL

NACA	α^{XFOIL}	$C_{L\,max}^{EXP}$	$\lvert\Delta C_p\rvert_{INV}$	$\lvert\Delta C_p\rvert_{VISC}$
0006	7.6°	0.85	12.4888	11.0791
0009	11.9°	1.32	14.9808	13.1859
0012	14.7°	1.59	14.0834	11.8816
1412	13.4°	1.57	11.3981	9.5804
2412	13.7°	1.67	11.5083	9.2498
2424	10.4°	1.28	4.0410	2.9981
4412	11.3°	1.64	7.1503	5.7869
4424	8.5°	1.33	3.4213	2.5771
23012	15.5°	1.74	11.9638	9.3930
23021	12.7°	1.48	4.9828	4.0022
23024	11.2°	1.30	4.5248	3.5734
64-208	9.4°	1.21	15.5322	14.0615
64_1-212	13°	1.56	15.3371	12.6382
64_4-221	13.2°	1.35	7.4725	5.7162

6.4 Pressure difference rule application

The *pressure difference rule* implementation consists in searching the angle of attack for which the pressure coefficient difference is equal to the critical value theorized by Valarezo and Chin for $Re = 6 \times 10^6$ and $M = 0.15$: this angle is expected to correspond to α_{stall}^{EXP} from Abbott and Von Doenhoff's experimental data.

$$|\Delta C_p| = |C_{p\,PEAK} - C_{p\,TE}| = 14 \tag{6.1}$$

To carry out this analysis, a simple MATLAB script (provided in Appendix.1) is created with the following steps:

1. Choose the interval of angles, in which perform the research, and growth step;
2. Assign an index i to each value in this range;
3. Create a file which contains the string commands to give to XFOIL, including the NACA airfoil name, the Reynolds and Mach numbers (if the viscous computation is requested), the angle of attack using its own assigned index and the command to save the data of the C_p distribution over the discretized profile points;
4. Execute XFOIL with the commands file for each index i;
5. Extract the C_p distribution for each angle i;

6. Compute $|\Delta C_p|_i = |C_{p\,PEAK} - C_{p\,TE}|_i$, where $C_{p\,PEAK}$ is the minimum value and $C_{p\,TE}$ is the value at the trailing edge;

7. Search the pressure coefficient distribution i which has the $|\Delta C_p|$ value closest to 14 $\implies$ $\alpha_i = \alpha_{stall}$.

Since in the previous section it has already been determined that the thick airfoils present a $|\Delta C_p|$ value much lower than the critical, the analysis is applied only to the airfoils with thickness less than 12% of the chord and it is performed with both inviscid and viscous conditions.

Table 6.5. Comparison between the experimental stall and the inviscid prevision of the stall, obtained with the *pressure difference rule*

NACA	α_{stall}^{EXP}	$C_{L\,max}^{EXP}$	$(\alpha_{stall}^{PREV})_{INV}$	$(C_{L\,max}^{PREV})_{INV}$
0006	9.1°	0.84	8.4°	0.9360
0009	13.3°	1.32	12°	1.3315
0012	16.5°	1.58	15.4°	1.6444
1412	14.7°	1.57	15°	1.6853
2412	17.3°	1.67	15.8°	1.7854
4412	14.3°	1.63	16.2°	1.8857
23012	17.3°	1.73	17.3°	1.8053
64-208	10.1°	1.20	9°	1.1677
64_1-212	15.2°	1.56	13°	1.5577

Table 6.6. Comparison between the experimental stall and the viscous prevision of the stall, obtained with the *pressure difference rule*

NACA	α_{stall}^{EXP}	$C_{L\,max}^{EXP}$	$(\alpha_{stall}^{PREV})_{VIS}$	$(C_{L\,max}^{PREV})_{VIS}$
0006	9.1°	0.84	8.6°	0.9574
0009	13.3°	1.32	12.4°	1.3705
0012	16.5°	1.58	16.5°	1.6972
1412	14.7°	1.57	16.4°	1.7538
2412	17.3°	1.67	18.8°	Stalled
4412	14.3°	1.63	24.3°	Stalled
23012	17.3°	1.73	18.7°	Stalled
64-208	10.1°	1.20	9.3°	1.2150
64_1-212	15.2°	1.56	14.2°	1.6197

As shown in Tables 6.5 and 6.6, the *pressure difference rule* generally produces some good predictions of the α_{stall}, in spite of what has been seen in the previous sections: this is probably due to the fact that small changes of the angle of attack involves significant variations of $|\Delta C_p|$.

The inviscid results (Table 6.5) can be defined satisfactory for every airfoils, because they forecast an angle of stall slightly advanced or similar to the experimental one, whereas the maximum lift coefficient turns out to be comparable only for the airfoils which have a well-approximated C_L-α curve.

The viscous case (Table 6.6), instead, is more accurate in the prediction of the symmetric and thin airfoils, but it goes wrong the cambered ones, also exceeding the experimental stall angle.

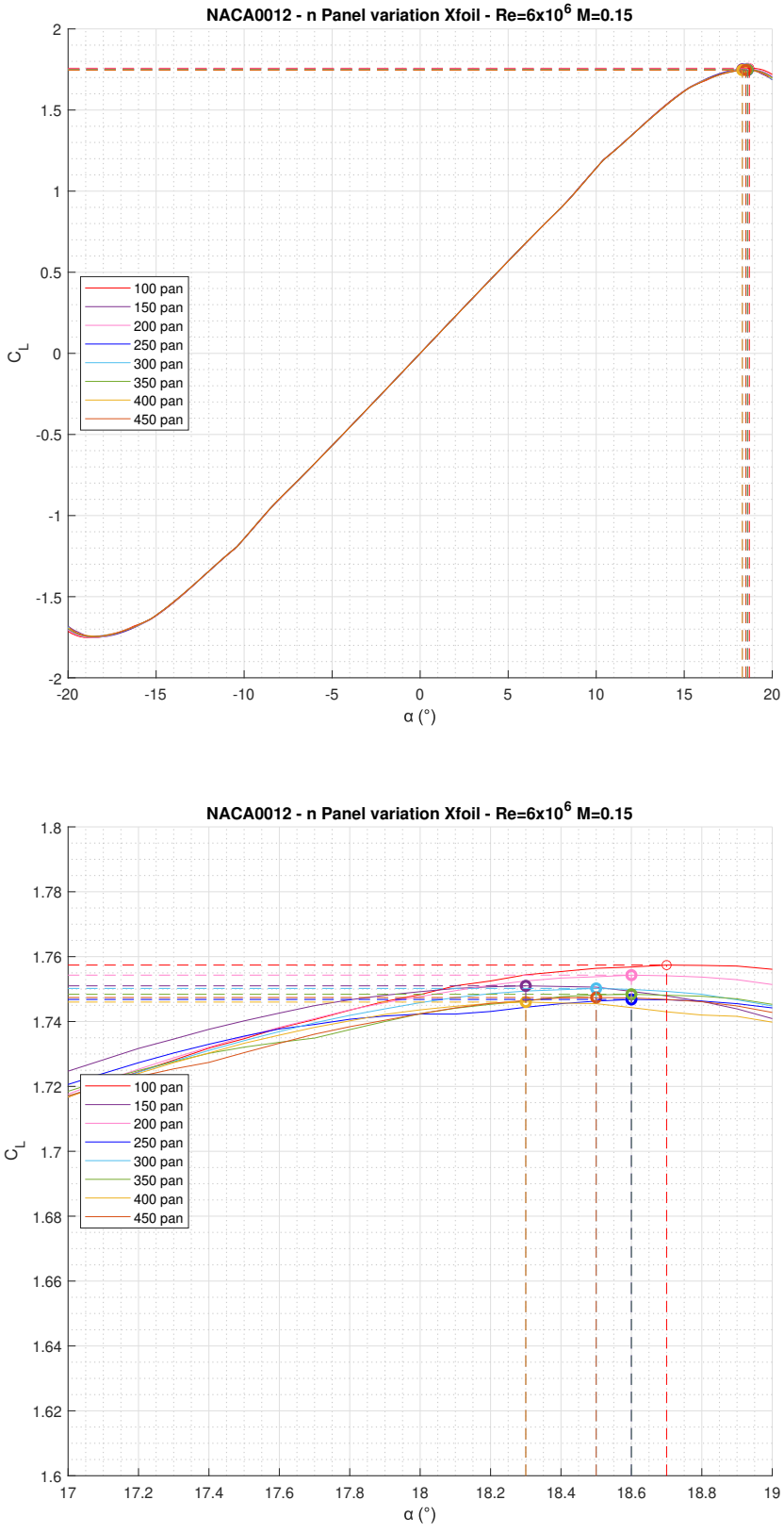

Figure 6.2. n_{panel} parameterization on lift coefficient versus angle of attack plot

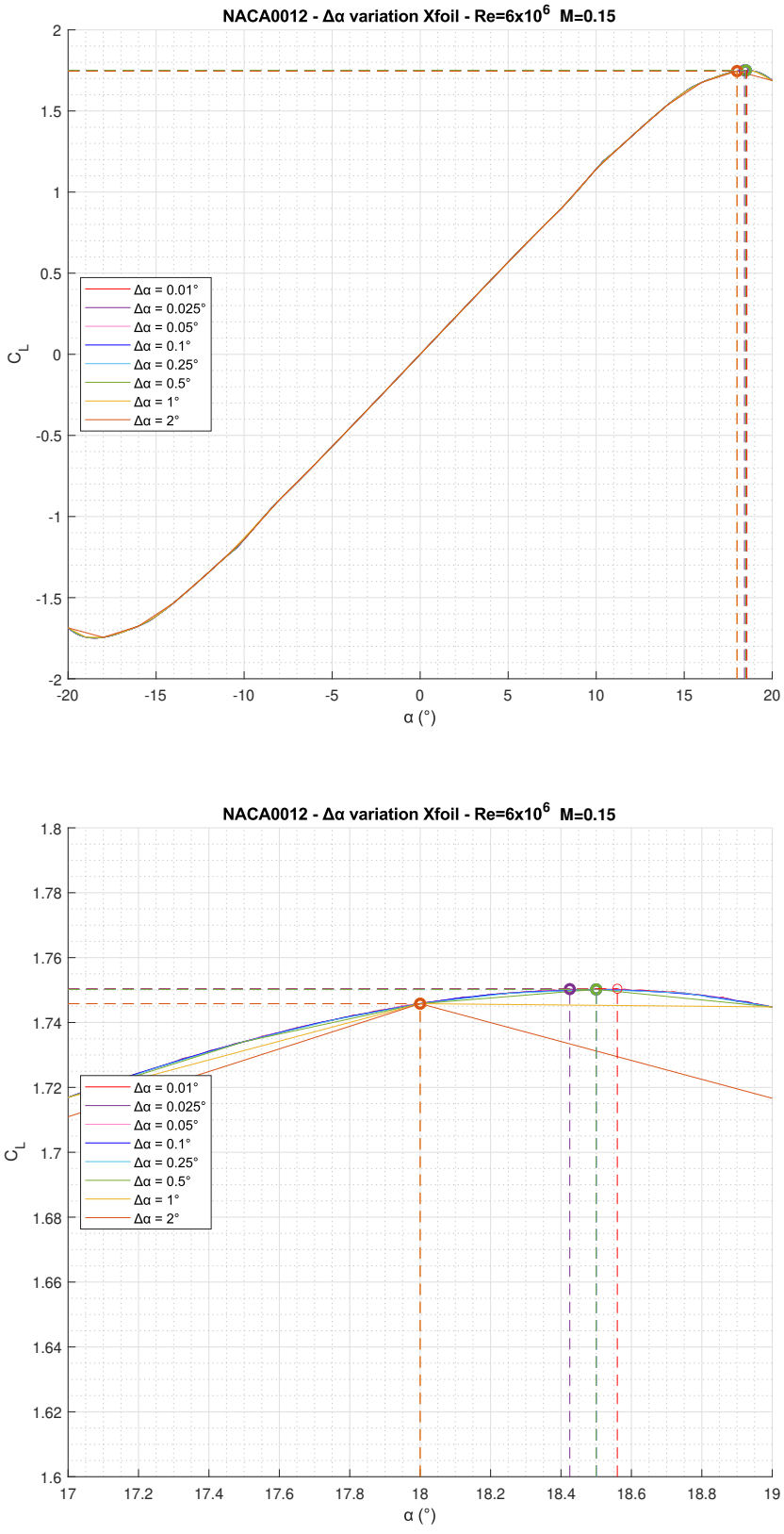

Figure 6.3. $\Delta\alpha$ parameterization on lift coefficient versus angle of attack plot

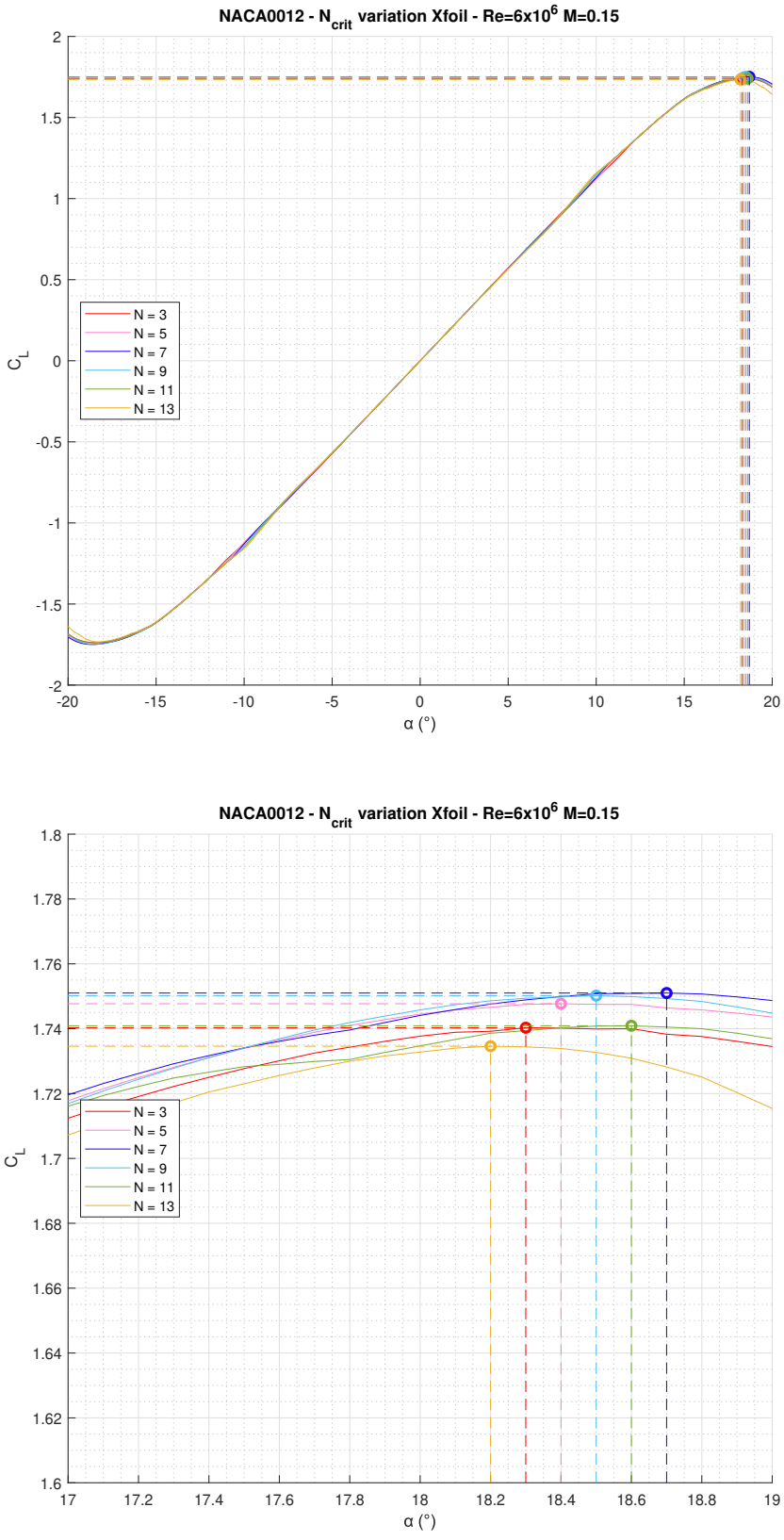

Figure 6.4. N_{crit} parameterization on lift coefficient versus angle of attack plot

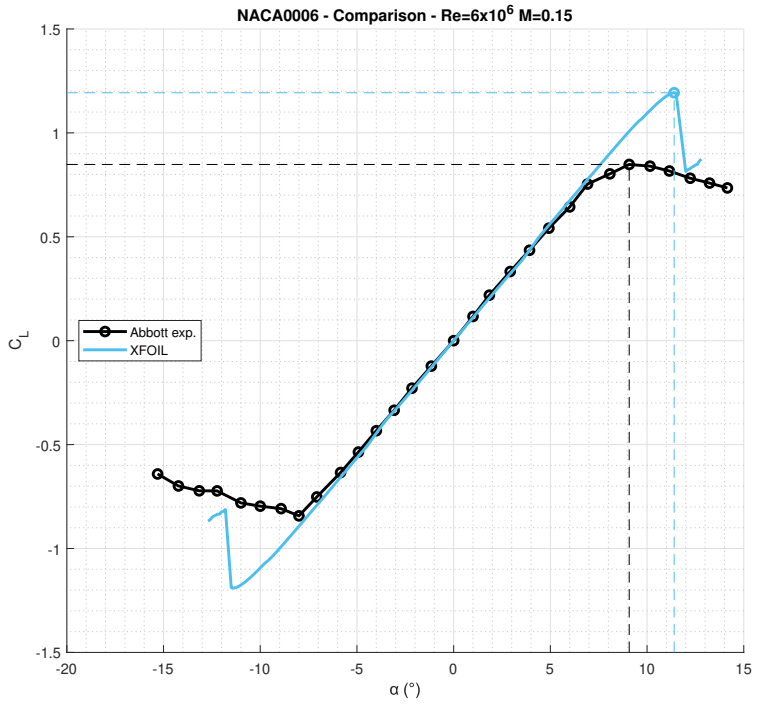

Figure 6.5. NACA0006 C_L-α curve comparison between experimental and computational data

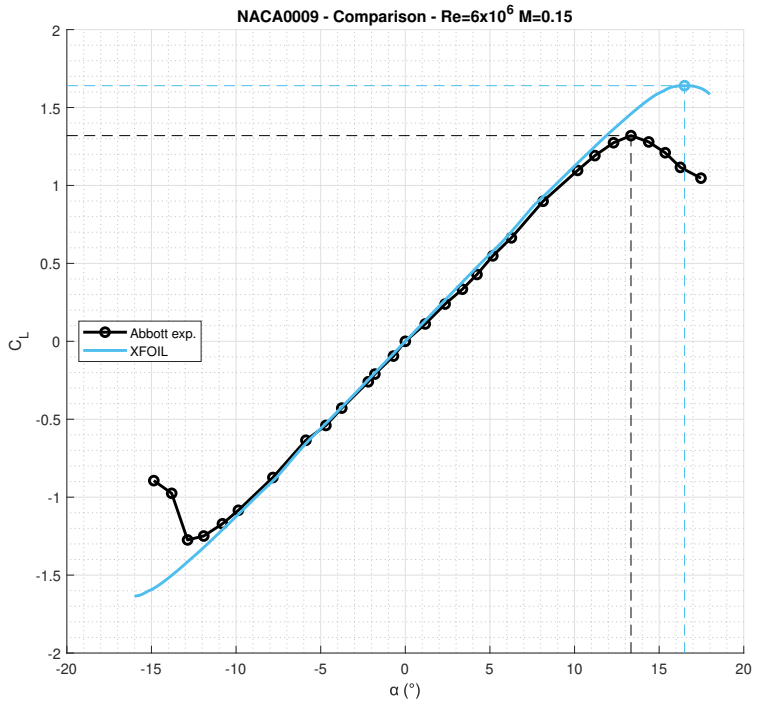

Figure 6.6. NACA0009 C_L-α curve comparison between experimental and computational data

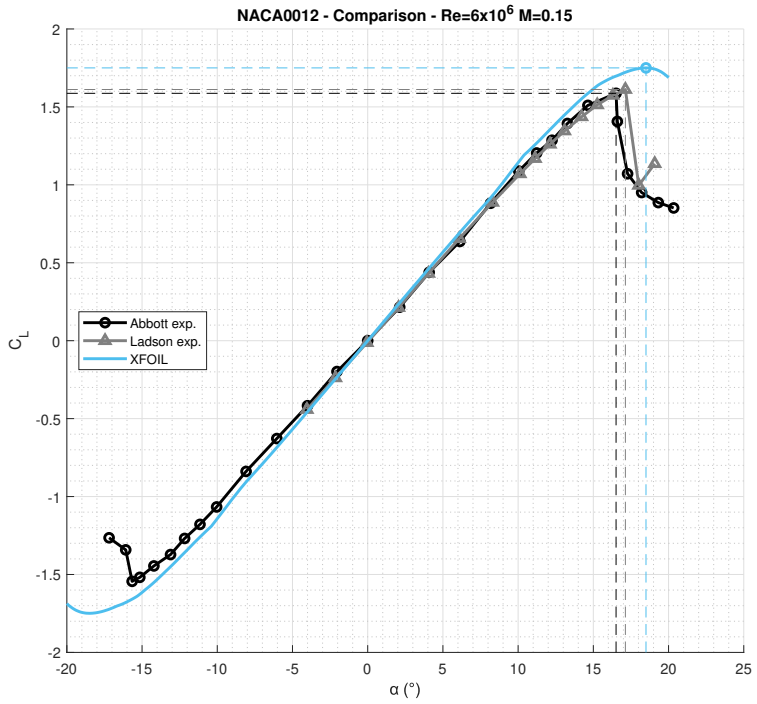

Figure 6.7. NACA0012 C_L-α curve comparison between experimental and computational data

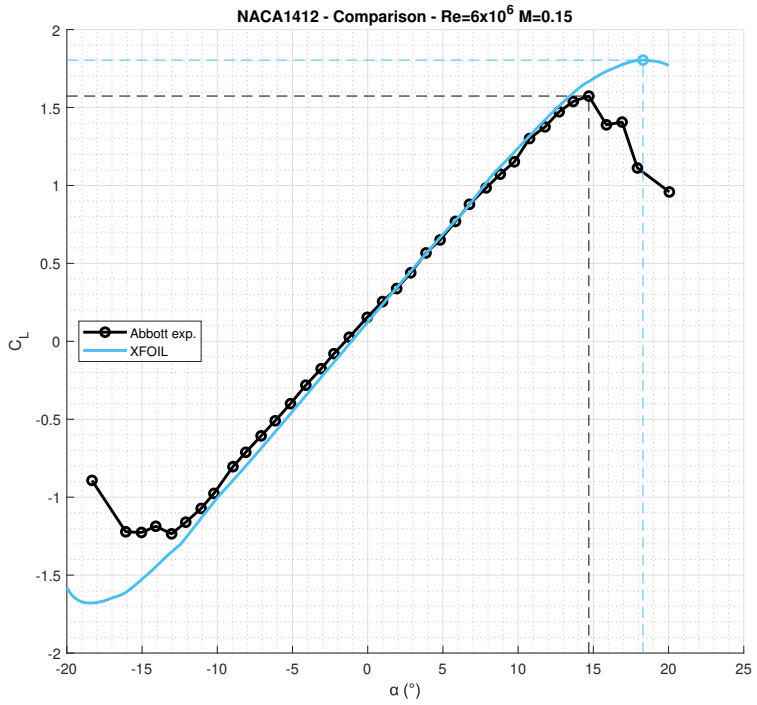

Figure 6.8. NACA1412 C_L-α curve comparison between experimental and computational data

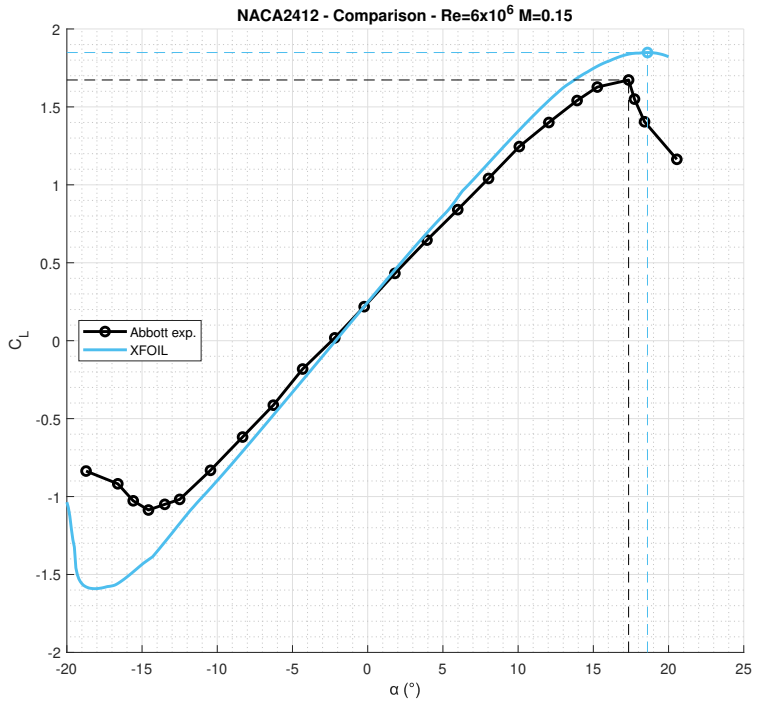

Figure 6.9. NACA2412 C_L-α curve comparison between experimental and computational data

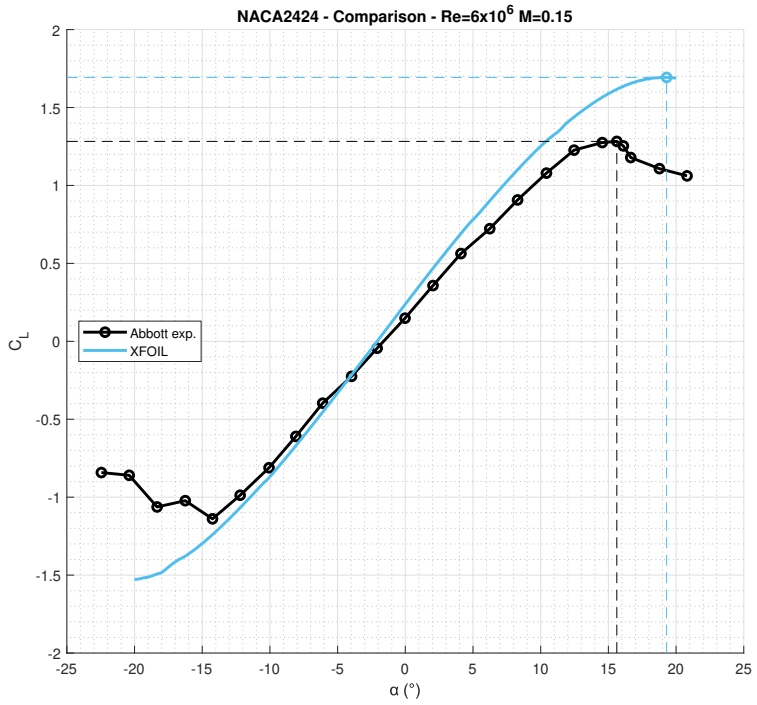

Figure 6.10. NACA2424 C_L-α curve comparison between experimental and computational data

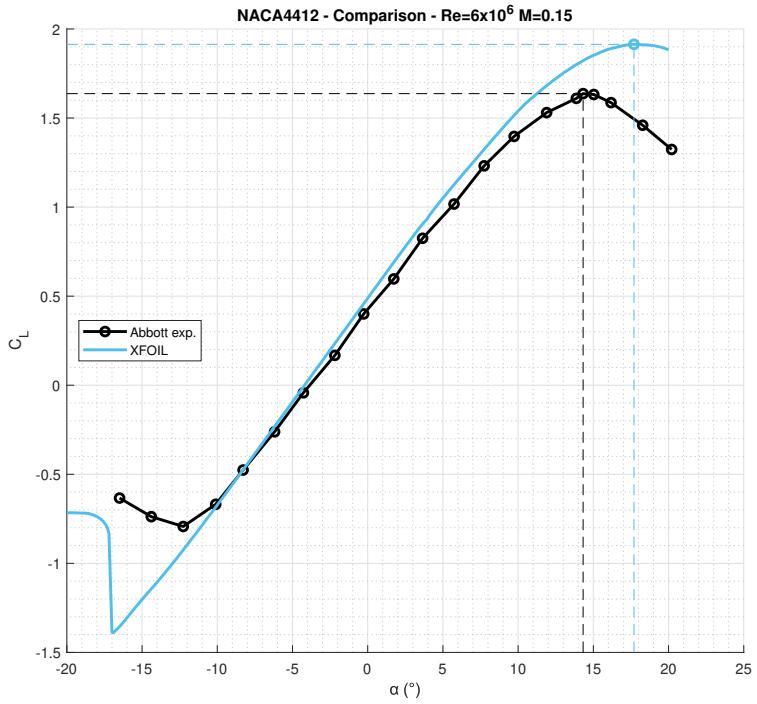

Figure 6.11. NACA4412 C_L-α curve comparison between experimental and computational data

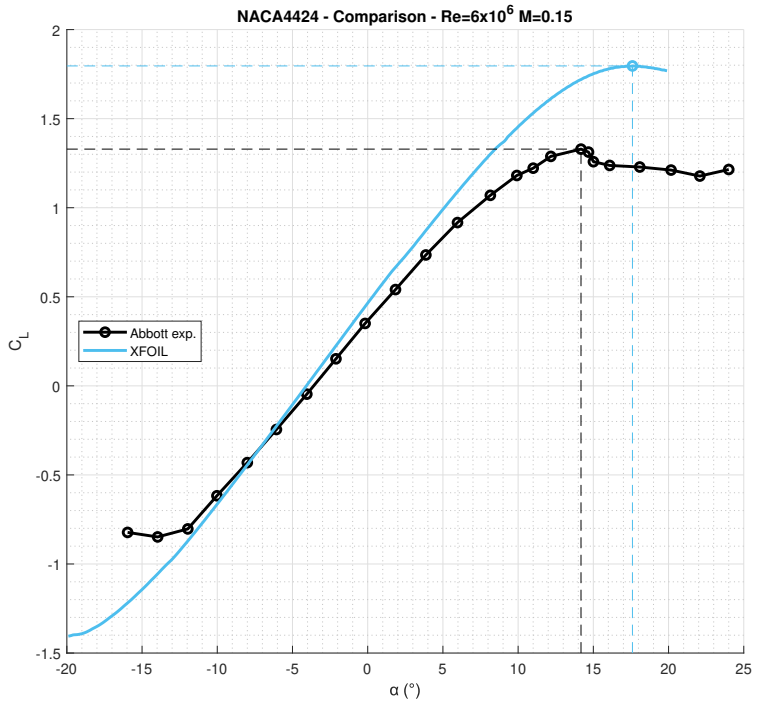

Figure 6.12. NACA4424 C_L-α curve comparison between experimental and computational data

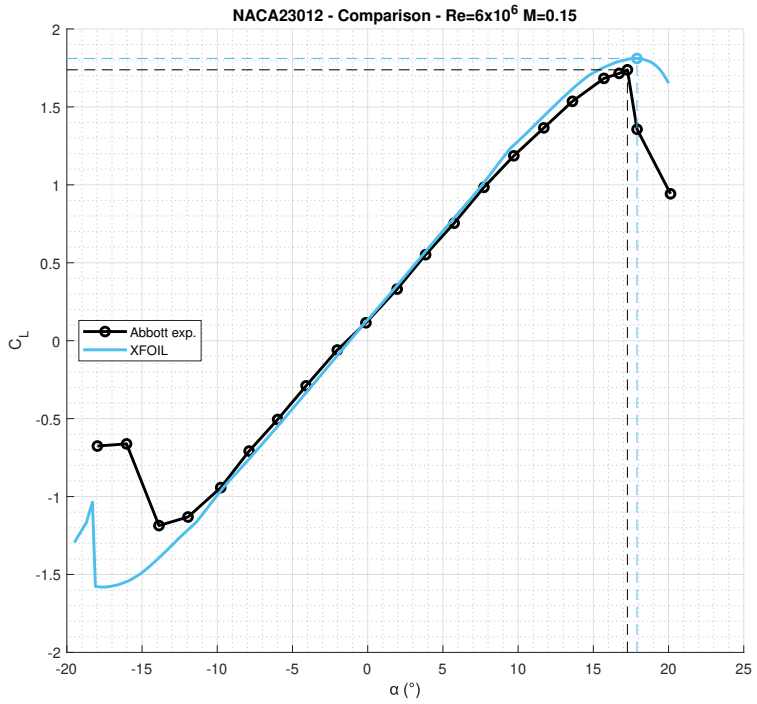

Figure 6.13. NACA23012 C_L-α curve comparison between experimental and computational data

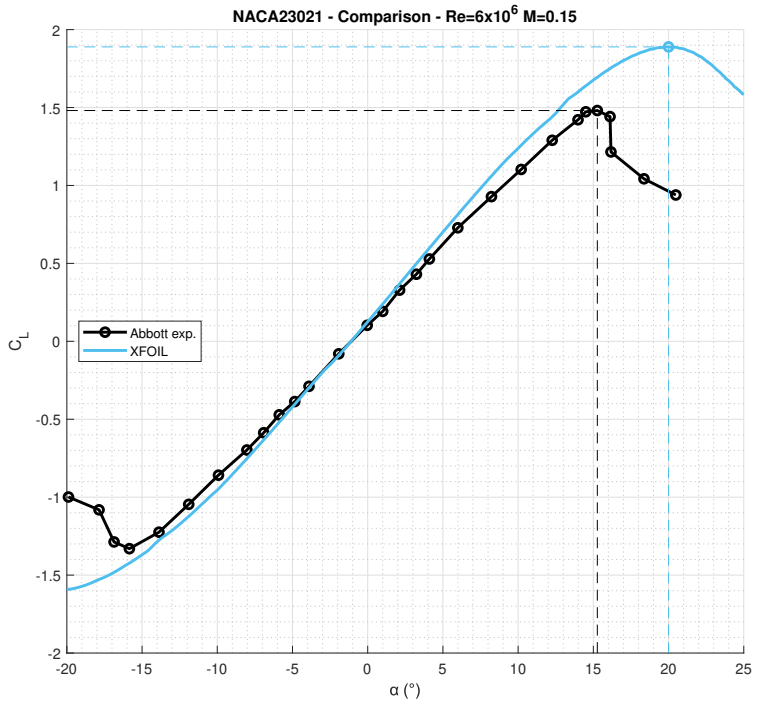

Figure 6.14. NACA23021 C_L-α curve comparison between experimental and computational data

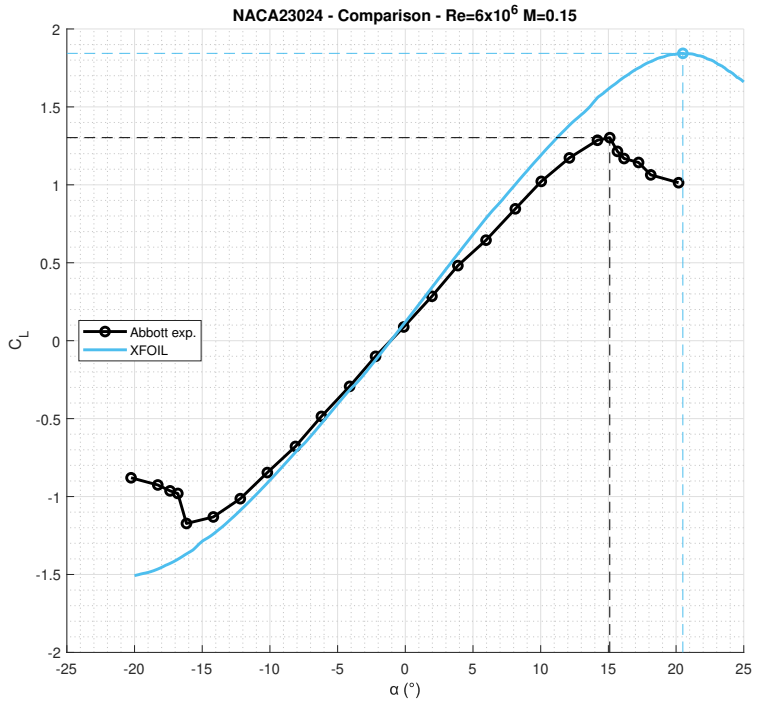

Figure 6.15. NACA23024 C_L-α curve comparison between experimental and computational data

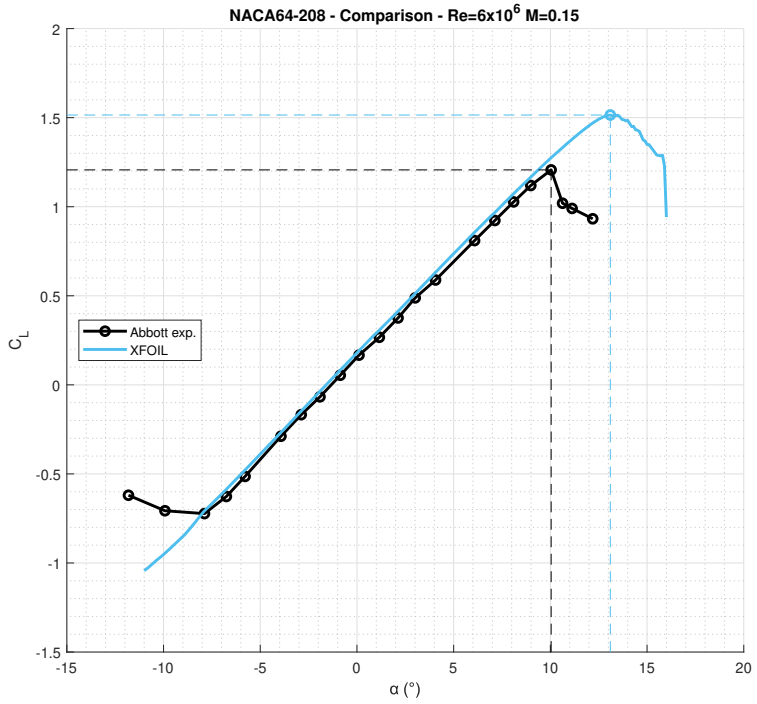

Figure 6.16. NACA64-208 C_L-α curve comparison between experimental and computational data

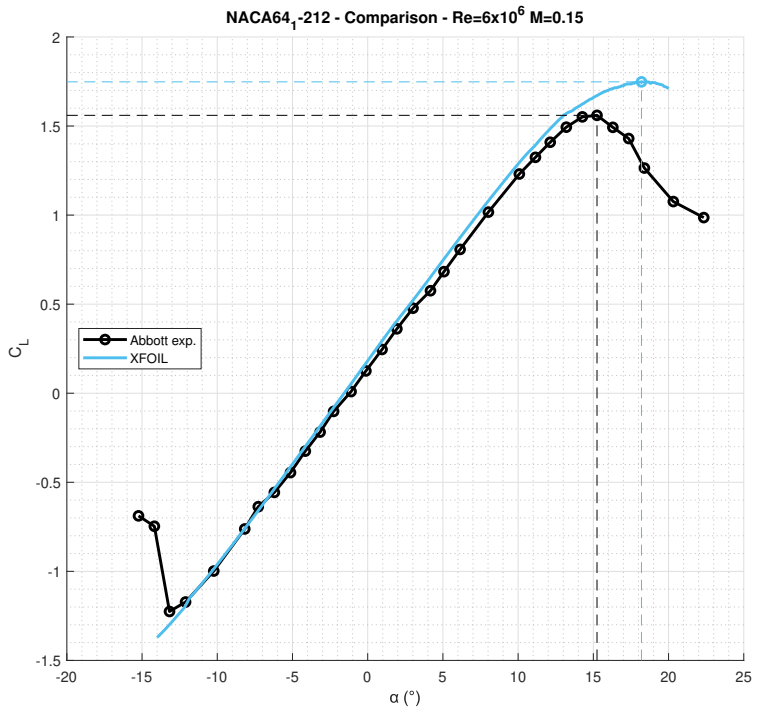

Figure 6.17. NACA64$_1$-212 C_L-α curve comparison between experimental and computational

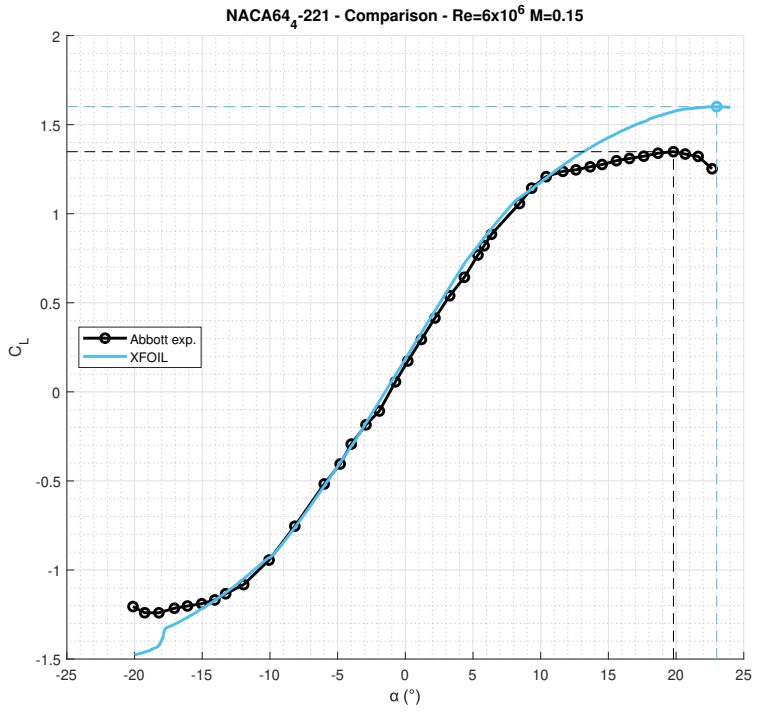

Figure 6.18. NACA64$_4$-221 C_L-α curve comparison between experimental and computational

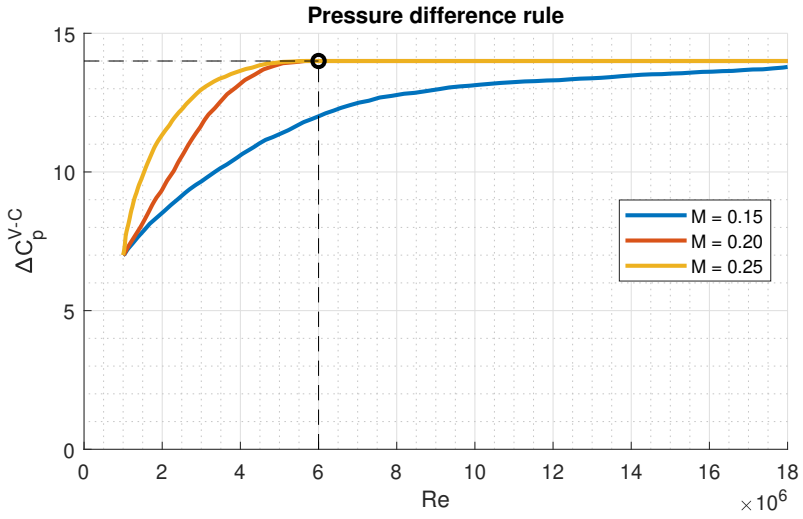

Figure 6.19. Pressure difference rule digitized with *WebPlotDigitizer*

Chapter 7

Modification of the method

Although the NACA airfoils investigated in this thesis are relatively few, this last chapter will try to propose an amendment of rule for the stall condition prevision, starting from the Valarezo and Chin Method and using the analysis performed in Chapter 6.

Having regard to the results displayed in Tables 6.2 and 6.4, the starting reasoning is to divide the method into two rules, one for thin airfoils ($< 12\%$ of the chord) and the other for thick airfoils ($> 21\%$ of the chord). A second partition is done on the prediction of the α_{stall} and of the $C_{L\,max}$: while the $|\Delta C_p|$ in Tab. 6.2 are obtained from the experimental stall angle and they best simulate its value, the data in 6.4 follow the experimental value of the maximum lift coefficient. For each case, the behaviour depending on the maximum thickness and the trend depending on the maximum camber are employed independently and only later they are reunited, to obtain the stall condition of the airfoil.

Since this is a method of forecasting, only the inviscid computations are used, because they have to be fast and cheap. The modification is only applied to the 4-digits and 5-digits families, since for the laminar airfoils cannot been recognized a behaviour clearly dependant on thickness and camber.

Moreover, it has to be reminded that all the previous analysis are conducted at $Re = 6 \times 10^6$ and $M = 0.15$ just for 2D airfoils, so this modification covers only a part of the Valarezo and Chin Method; however, the study can be repeated with different parameters and it can be applied to find a more complete amendment to the pressure difference rule.

7.1 Thin airfoils

In order to consider the thickness contribution, only the symmetric airfoils -NACA0006, NACA0009 and NACA0012- are considered and their data from the Tables 6.2 and 6.4 are displayed in Figures 7.1 and 7.2, where the airfoils are sorted by increasing thickness on the x axis.

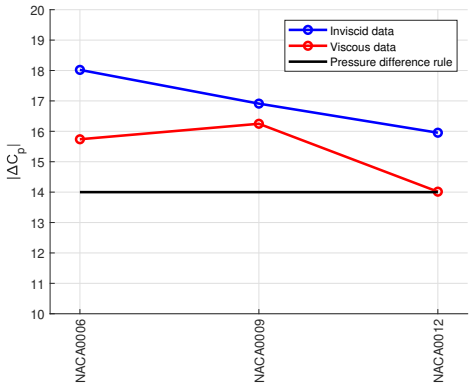

Figure 7.1. $|\Delta C_p|$ data from the Table 6.2

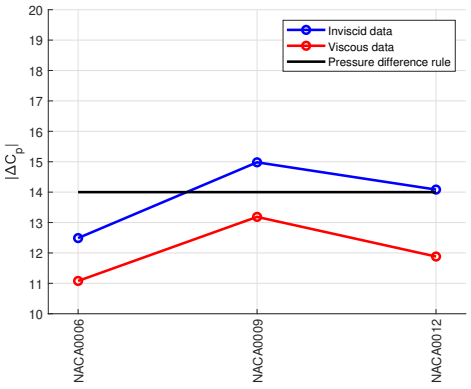

Figure 7.2. $|\Delta C_p|$ data from the Table 6.3

From the same tables, the graphs 7.3 and 7.4 are obtained for the airfoils with thickness equal to 12% of the chord, i.e. NACA0012, NACA1412, NACA2412, NACA4412 and NACA23012. Here the airfoils are ordered by increasing maximum camber.

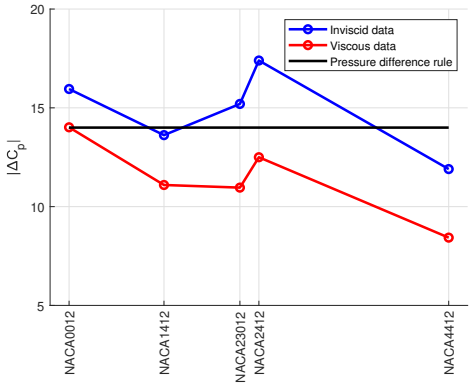

Figure 7.3. $|\Delta C_p|$ data from the Table 6.2

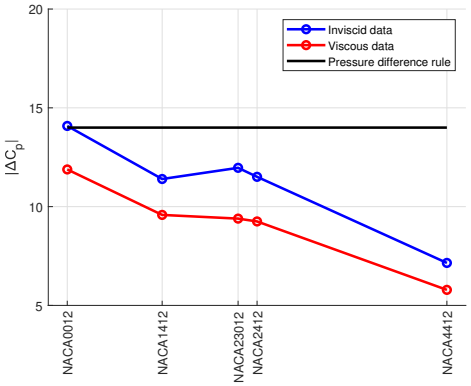

Figure 7.4. $|\Delta C_p|$ data from the Table 6.3

By interpolating these last plots, two new graphs in figures 7.5 and 7.6 are derived and they are used as the starting point of the modified method: after choosing the airfoil whose the stall condition has to be found, its initial $|\Delta C_p|$ values are obtained from the curves in correspondence to its maximum camber. The first value $|\Delta C_p|^{\alpha}_{init}$ will be used in the next step to predict the stall angle of attack, while the second $|\Delta C_p|^{C_L}_{init}$ will be used for the maximum lift coefficient. It should be noticed that the curves are dashed for some sections, because their trends are not known, due to the lack of information.

Then, these starting values just found are multiplied for an amplification factor f, in order to get the final $|\Delta C_p|$. The amplification factor f depends on the airfoil thickness and it is different according to whether α_{stall} or $C_{L\,max}$ has to be predicted, as shown in Figures 7.5 and 7.6. Indeed, f_α and f_{C_L} derive respectively from the data depicted in Figure 7.1 and 7.2, divided by the respective value of $|\Delta C_p|$ of the

NACA0012, which is taken as reference, since it is present in both the steps (being both symmetrical and 12% thick).

$$|\Delta C_p|^{final} = |\Delta C_p|^{init} \cdot f \qquad \text{where} \qquad f = \frac{|\Delta C_p|}{|\Delta C_p|_{NACA0012}} \tag{7.1}$$

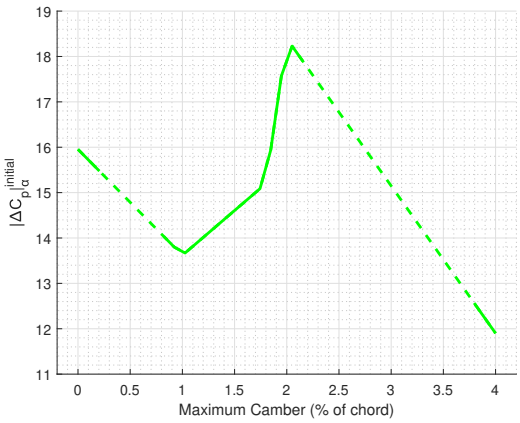

Figure 7.5. Plot of $|\Delta C_p|_\alpha^{init}$ versus maximum camber: first step of the modified criterion to predict the α_{stall}

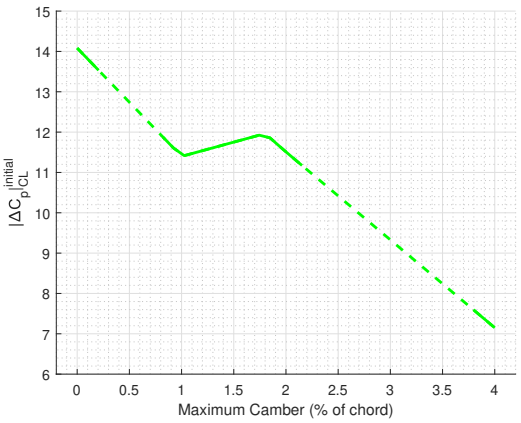

Figure 7.6. Plot of $|\Delta C_p|_{C_L}^{init}$ versus maximum camber: first step of the modified criterion to predict the $C_{L\,max}$

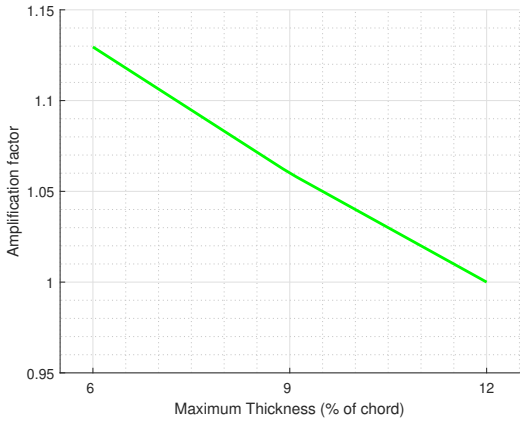

Figure 7.7. Plot of amplification factor versus maximum thickness: second step of the modified criterion to predict the α_{stall}

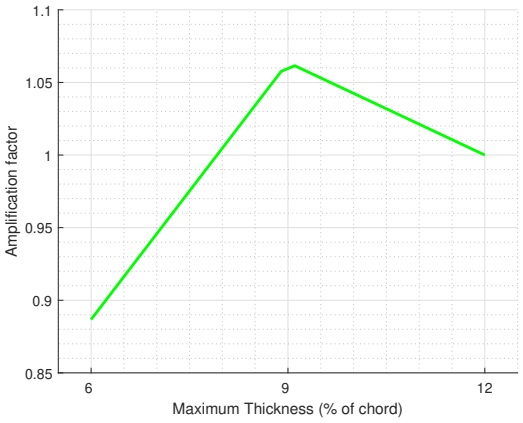

Figure 7.8. Plot of amplification factor versus maximum thickness: second step of the modified criterion to predict the $C_{L\,max}$

Finally, the last step of the criterion is, as usual, the computation of the angle at which the airfoil assumes the $|\Delta C_p|^{final}$. This operation is carried out with the XFOIL program, using the same procedure (A.1) described in the last section of Chapter 6. The algorithm, executed at inviscid condition, directly provides the

predicted α_{stall}, if the input is $|\Delta C_p|_{\alpha}^{final}$; whereas, if the input is $|\Delta C_p|_{C_L}^{final}$, the expected $C_{L\,max}$ has to be computed at the output α, always with XFOIL.

7.2 Thick airfoils

In this case, the new criterion is even more restricted than the previous, due to the very few considered airfoils. However, since the $|\Delta C_p|$ values for thick airfoils, found during the analysis in Chapter 6, differ very much from the critical value of 14, theorized by Valarezo and Chin, the amendment is useful and efficient.

The reasoning and the procedure are the same of the thin airfoils case, always splitting the search for α_{stall} and $C_{L\,max}$: looking at the data in Figures 7.11 and 7.12, the plots 7.13 and 7.14 are obtained, while the amplification factor trends 7.15 and 7.16 are found from the graphs 7.9 and 7.10. This time, the reference airfoil, which appears in both analysis on camber and thickness, is the 5-digits NACA23024.

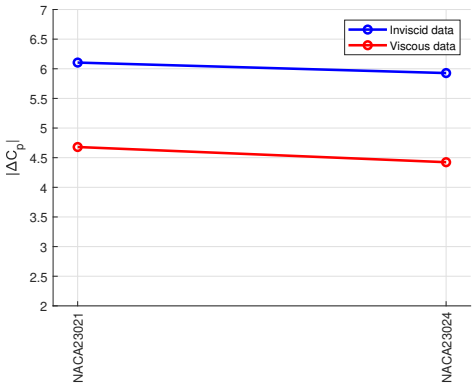

Figure 7.9. $|\Delta C_p|$ data from the Table 6.2

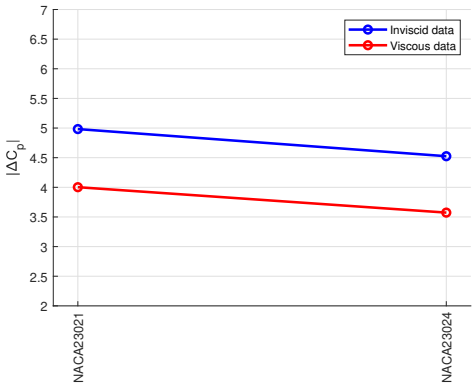

Figure 7.10. $|\Delta C_p|$ data from the Table 6.3

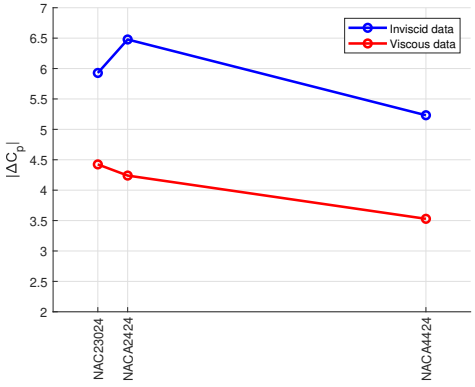

Figure 7.11. $|\Delta C_p|$ data from the Table 6.2

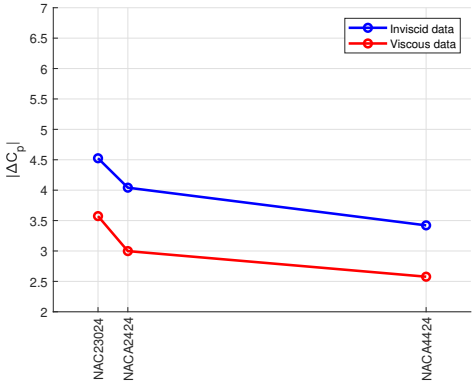

Figure 7.12. $|\Delta C_p|$ data from the Table 6.3

Therefore, choosing the thick airfoil, whose stall needs to be predicted, maximum camber and maximum thickness have to be computed. The $|\Delta C_p|^{init}$ is given by Figures 7.13 and 7.14 and f by Figures 7.15 and 7.16: so the $|\Delta C_p|^{final}$ can be computed and used in the XFOIL inviscid algorithm to obtain the stall angle and the angle correspondent to the $C_{L\,max}$. At this point, unlike the thin airfoil case, in order to predict the maximum lift coefficient, it is more accurate the viscous calculation.

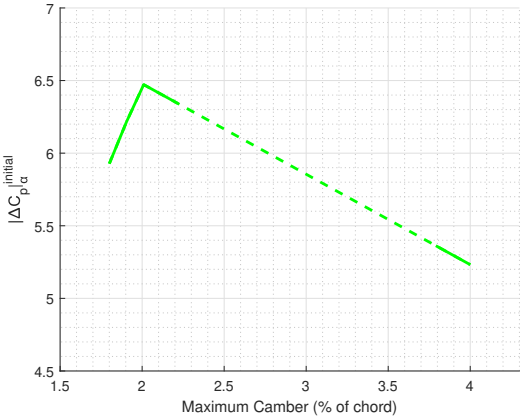

Figure 7.13. Plot of $|\Delta C_p|^{init}_{\alpha}$ versus maximum camber: first step of the modified criterion to predict the α_{stall}

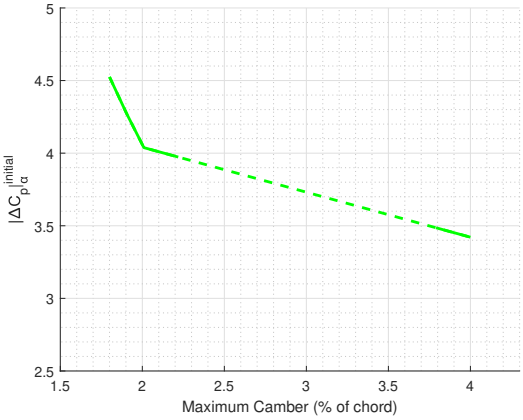

Figure 7.14. Plot of $|\Delta C_p|^{init}_{C_L}$ versus maximum camber: first step of the modified criterion to predict the $C_{L\,max}$

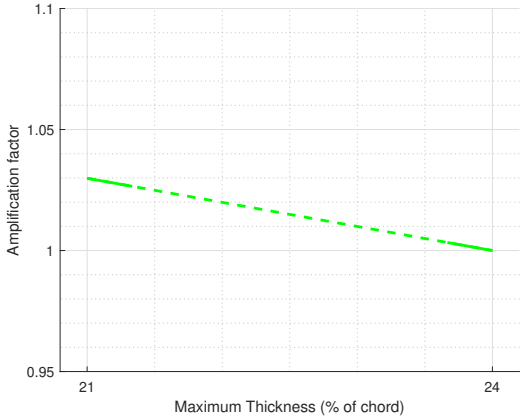

Figure 7.15. Plot of amplification factor versus maximum thickness: second step of the modified criterion to predict the α_{stall}

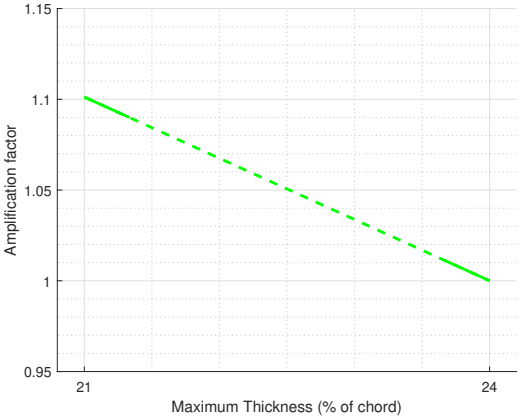

Figure 7.16. Plot of amplification factor versus maximum thickness: second step of the modified criterion to predict the $C_{L\,max}$

7.3 Modified pressure difference rule application

Finally the amendments are tested, through the MATLAB code used for pressure difference rule application (Appendix.1), in four different NACA airfoils, i.e. NACA1410, NACA2408, NACA2421 and NACA4421. The results are compared with the usual experimental data by Abbott and and Von Doenhoff. A diagram is used to represent the processes described in the previous sections and to show the results for each airfoil.

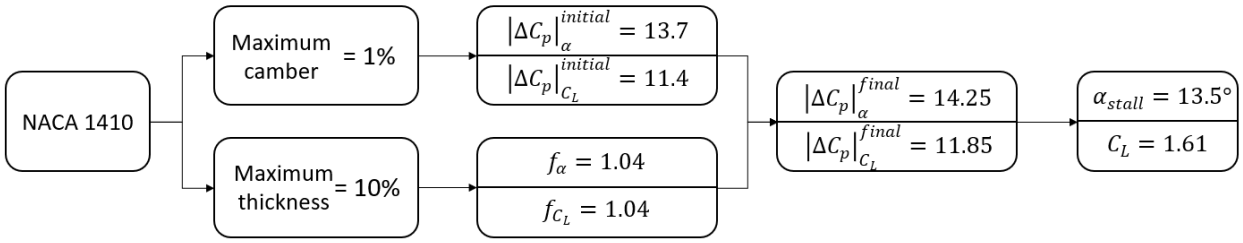

Figure 7.17. NACA1410 process diagram of the modified pressure difference rule

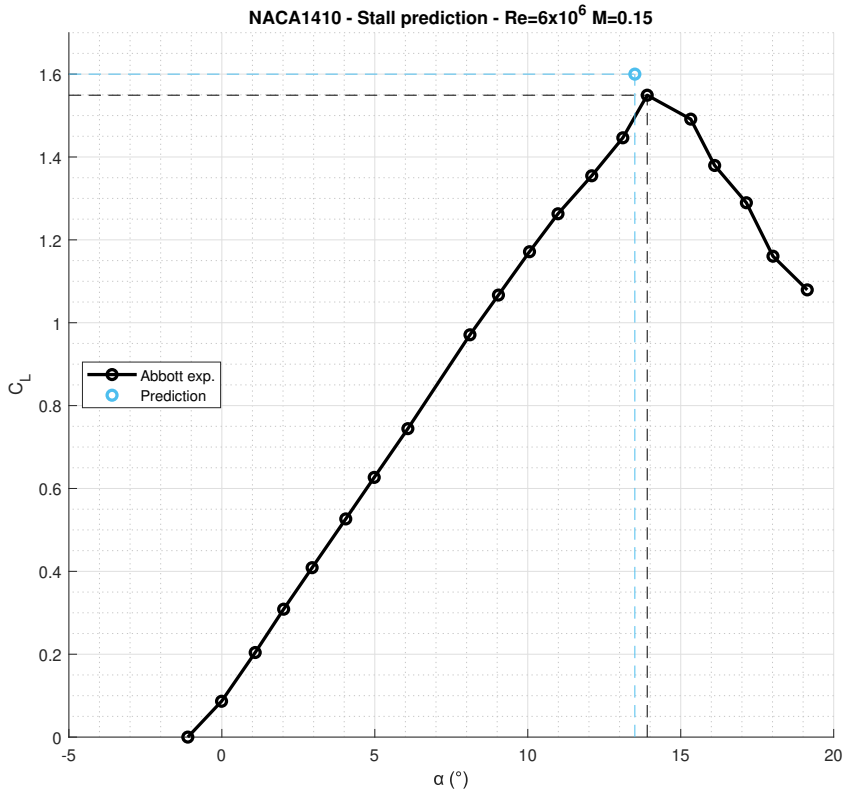

Figure 7.18. NACA1410 stall prediction with the modified method compared with the experimental data by Abbott and and Von Doenhoff

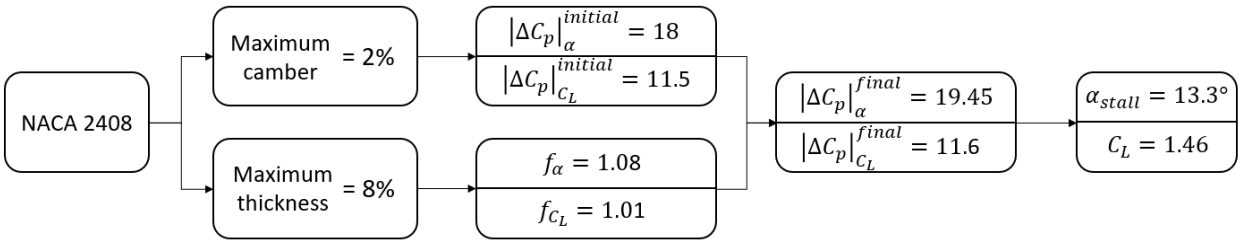

Figure 7.19. NACA2408 process diagram of the modified pressure difference rule

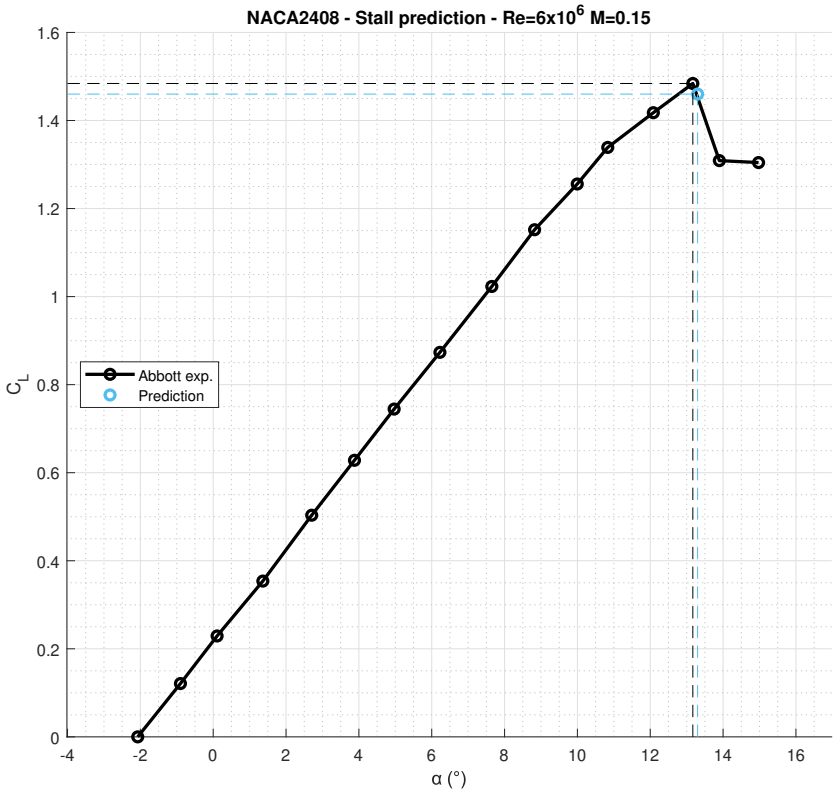

Figure 7.20. NACA2408 stall prediction with the modified method compared with the experimental data by Abbott and and Von Doenhoff

As depicted in Figures 7.18 and 7.20, the method for the thin airfoils seems to well approximate the stall: indeed, the errors for the NACA1410 are about the 3% on both the α_{stall} and the $C_{L\,max}$, while for the NACA2408 they are respectively the 1% and the 1.5%.

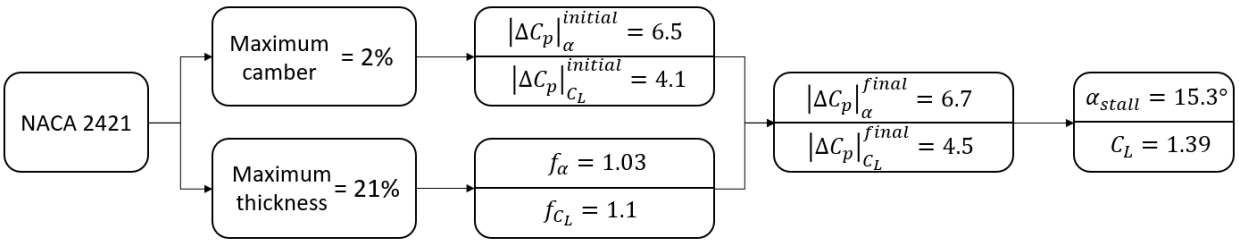

Figure 7.21. NACA2421 process diagram of the modified pressure difference rule

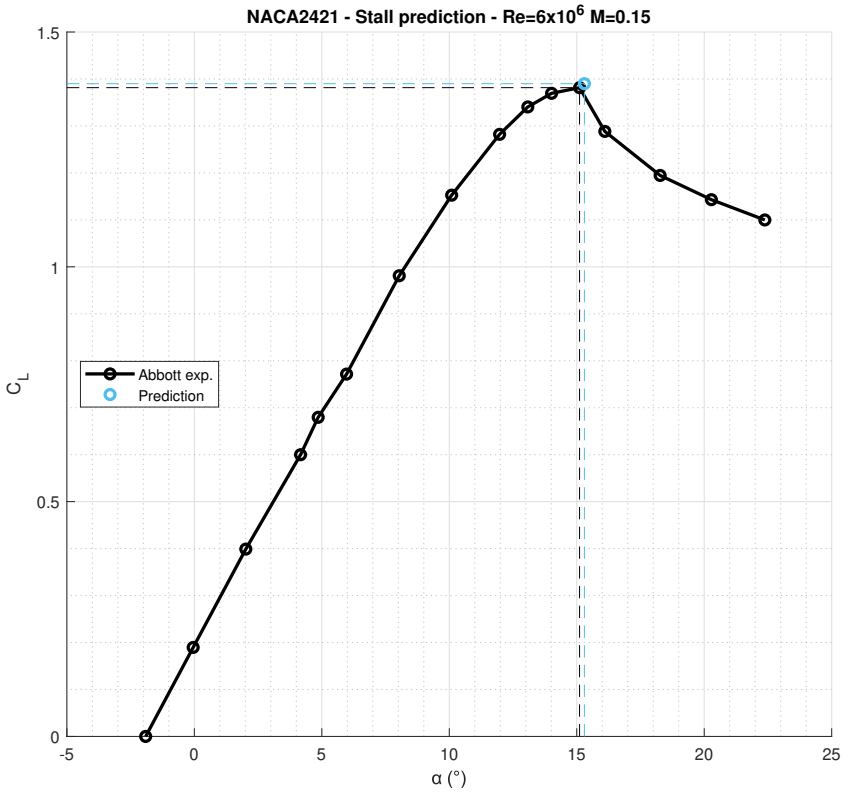

Figure 7.22. NACA2421 stall prediction with the modified method compared with the experimental data by Abbott and and Von Doenhoff

The Figures 7.22 and 7.24 show that the rule works also in the case of thick airfoil, even if results for the NACA4421 are not so accurate. The deviations of the latter airfoil are of the 5% for the stall angle and of the 4% for the maximum lift coefficient.

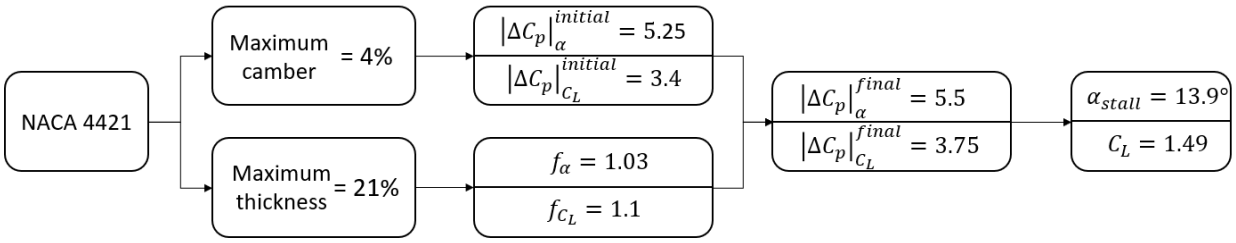

Figure 7.23. NACA4421 process diagram of the modified pressure difference rule

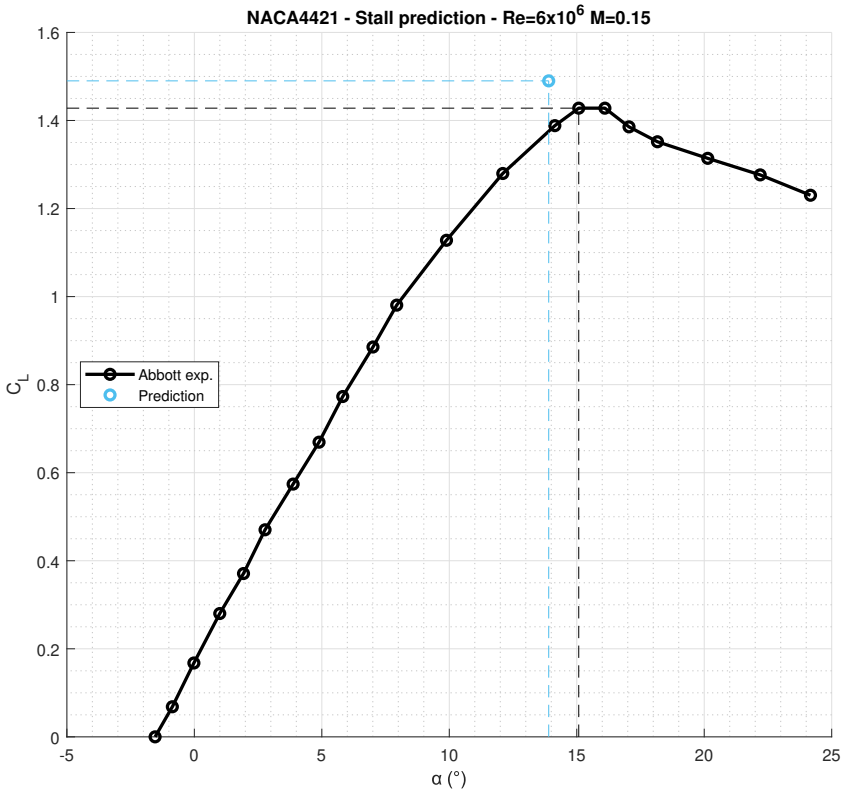

Figure 7.24. NACA4421 stall prediction with the modified method compared with the experimental data by Abbott and and Von Doenhoff

Conclusions

The Valarezo-Chin method for the prediction of the maximum lift is a fast criterion for the starting phase of an aircraft, thanks to the few steps and the use of a low-fidelity computational method. According to the authors, it has a wide validity field, since the rule applies to several Reynolds and Mach numbers and to bi-dimensional and three-dimensional airfoils, both simple and multiple. However, in this thesis, it is analyzed just at $Re = 6 \times 10^6$ and $M = 0.15$ and only for a few 2D NACA airfoils; so the results presented are limited and relatively reliable.

XFOIL is a very valuable tool in computing the aerodynamic features of bi-dimensional airfoils, since its accurate results, its low variability to the input parameters changes and its low computational cost. However, getting closer to the stall, the accuracy of the results depends on the geometric characteristics of the airfoil in examination and the discrepancy with the experimental data generally grows with thickness and camber. Nevertheless, XFOIL is suitable to be used as panel method in Valarezo-Chin method, paying the necessary attention to its lacks.

The *Pressure difference rule* at $Re = 6 \times 10^6$ and $M = 0.15$, in light of the analysis carried out, turns out to be not very reliable, with results very dependent on airfoils: the pressure coefficient difference between the peak and the trailing edge equal to a fixed value of 14 seems a bit inaccurate for thin airfoils, but completely erroneous for thick and heavily curved airfoils. Since in the first case, the errors tend to anticipate the stall, the rule can be considered a a good engineering technique to study the aerodynamic characteristics of the airfoils in the preliminary design phase.

Furthermore, the suggested amendment to the rule appears to be very precise for the 4-digits and 5-digits NACA airfoils, with both α_{stall} and $C_{L\,max}$ deviations of about 1% with respect of the experimental data. These excellent results are counterbalanced by the specific use and the limited data. Due to these limits, the modification cannot be considered as an improvement over the Valarezo-Chin criterion, but as a starting point and a basis idea for a more accurate method. Indeed, it is not excluded the amendment extension to other airfoil, both NACA and of different types, and to wide range of Reynolds and Mach numbers.

Bibliography

[1] I.H. Abbott and A.E. Von Doenhoff. *Theory of Wing Sections, Including a Summary of Airfoil Data*. Dover Books on Aeronautical Engineering Series. Dover Publications, 1959.

[2] I.H. Abbott, A.E. Von Doenhoff, and Louis S. Stivers Jr. Summary of airfoil data - report no. 824. 1945.

[3] Ladson Charles L., Jr Cuyler W. Brooks, Hill Acquilla S., and Sproles Darrell W. Computer program to obtain ordinates for NACA airfoils. Technical report, 1996.

[4] Mark Drela. Xfoil: An analysis and design system for low reynolds number airfoils. volume 54, 06 1989.

[5] ESDU. The low-speed stalling characteristics of aerodynamically smooth airfoils. October 1966.

[6] Donald E. Gault. A correlation of low-speed, airfoil-section stalling characteristics with reynolds number and airfoil geometry. 1957.

[7] George B Mccullough and Donald E. Gault. Examples of three representative types of airfoil-section stall at low speed. 1951.

[8] Christopher L. Rumsey and Jeffrey P. Slotnick. Overview and summary of the second AIAA high-lift prediction workshop. *Journal of Aircraft*, 52(4):1006–1025, 2015.

[9] Christopher L. Rumsey and Susan X. Ying. Prediction of high lift: review of present CFD capability. *Progress in Aerospace Sciences*, 38(2):145–180, February 2002.

[10] B. Singh. A medium-fidelity method for rapid maximum lift estimation, 2017.

[11] A. M. O. Smith. High-lift aerodynamics. *Journal of Aircraft*, 12(6):501–530, 1975.

[12] Walter O. Valarezo and Vincent D. Chin. Method for the prediction of wing maximum lift. *Journal of Aircraft*, 31(1):103–109, 1994.

[13] J. van Ingen. The eN Method for Transition Prediction. Historical Review of Work at TU Delft. 2008.

[14] Roelof Vos and Saeed Farokhi. *Introduction to Transonic Aerodynamics*. Springer Netherlands, 2015.

Sitography

[15] WebPlotDigitizer. https://automeris.io/WebPlotDigitizer/

[16] NACA airfoil, Wikipedia. https://en.wikipedia.org/wiki/NACA_airfoil

Appendix

.1 MATLAB script for the pressure difference rule implementation

The MATLAB code used for the pressure difference rule application in Sections 6.4 and 7.3 is provided, in order to make it possible to replicate the results. The definitions of the variables and the main passages are commented in the code itself.

```
%% Pressure difference rule implementation
% It consists in searching the angle of attack for which the
% pressure coefficient difference is equal to a critical value.
% In order to make the script work, it must be saved in the same
% directory of the executable xfoil.exe.

clear all
close all
if not(isdir('./Cpvariation')), mkdir('./Cpvariation'); end

%=====================================================================
%% Commands to XFOIL
% Create a file with the inputs to insert in XFOIL

alpha = 0:0.1:20;    % Angle of attack interval where to search the
                     % critical pressure coefficient difference
                     % which corresponds to the stall;
N = length(alpha);
i = 1:N;
commands = {
 'naca 0012'         % Airfoil to be studied - only 4-digits and
                     % 5-digits NACA are supported; for different
                     % airfoils use the input 'load airfoil.dat',
                     % where airfoil.dat contains the coordinates of
                     % the profile;
 'ppar'
 'n 300'             % Number of panels;
 ''
 ''
 'oper'
 'iter 300'          % Number of iterations;
```

```
%  'v 6e6'          % Reynolds number for the viscous option if
                    % desired;
%  'm .15'          % Mach number if the viscous option is active;
 sprintf(['a %.3f\n' ...
 'cpwr ./Cpvariation/cp(%d).dat\n'], [alpha; i])
 'quit'
};

%=====================================================================
%% Run Xfoil

id = fopen('comandi.dat', 'w+');
fprintf(id, '%s\n', commands{:});
fclose(id);

!xfoil.exe < comandi.dat

%=====================================================================
%% Reading data

data = cell(1, N);
Cppeak = zeros(N, 1);    % Initialize the vector of minimum pressure
                         % coefficients for each angle;
Cpte = zeros(N, 1);      % Initialize the vector of trailing edge
                         % pressure coefficients for each angle;
for i = 1:N
 foo = importdata(sprintf('./Cpvariation/cp(%d).dat', i), ' ', 3);
 data{i} = foo.data(:, :, :);
 xyCp = cell2mat(data([i]));
 Cp = xyCp(:, 3);
 minCp = find(Cp==min(Cp));
 Cppeak(i, 1) = Cp(minCp(1));
 Cpte(i, 1) = Cp(1);
end

%=====================================================================
%% Post-processing

DeltaCp = abs(Cppeak-Cpte); % Compute the pressure coefficient
                            % difference between minimum peak and
                            % trailing edge;
DCp_critical = 14;       % Critical value of the pressure coefficient
                         % difference chosen by the user - the value
                         % theorized by Valarezo and Chin is 14;
[nearest, idx] = min(abs(DeltaCp-DCp_critical));
alfa_stall_predict = alpha(idx);    % Predicted stall angle;
```